International Journal of Biological Macromolecules 319 (2025) 145388

Contents lists available at ScienceDirect

International Journal of Biological Macromolecules

journal homepage: www.elsevier.com/locate/ijbiomac

MXene-modified PMMA/chitosan composite e-skin scaffold: Bioelectronic and antibacterial assessment

Berfin Gürbüz [a,b], Fatih Ciftci [a,c,d,*], Ali Can Özarslan [e,f], Bahar Akyuz Yilmaz [g]

[a] Department of Biomedical Engineering, Fatih Sultan Mehmet Vakıf University, Istanbul, Turkey
[b] Biomedical Electronic Design Application and Research Centre (BETAM), Fatih Sultan Mehmet Vakıf University, Istanbul, Turkey
[c] BioriginAI Research Group, Department of Biomedical Engineering, Fatih Sultan Mehmet Vakıf University, Istanbul, Turkey
[d] Department of Technology Transfer Office (TTO), Fatih Sultan Mehmet Vakıf University, Istanbul, Turkey
[e] Faculty of Engineering, Department of Metallurgical and Materials Engineering, Istanbul University-Cerrahpasa, Turkey
[f] Health Biotechnology Joint Research and Application Center of Excellence, Istanbul, Turkey
[g] Faculty of Science, Department of Molecular Biology and Genetics, Aksaray University, Aksaray, Turkey

ARTICLE INFO

Keywords:
Composite
E-skin scaffold
MXene
PMMA
Chitosan
Antibacterial

ABSTRACT

In tissue engineering, e-skin patches serve as wearable wound dressings for healing. In this study, electrospun nanofiber composites were developed by integrating PMMA, MXene, and chitosan (CS) to fabricate multifunctional e-skin scaffolds. The resulting PMMA–MXene–CS composite e-skin scaffolds exhibited a uniform fibrous morphology with average diameters of 600 ± 50 nm and high porosity (>85 %), providing an optimal microenvironment for tissue interfacing. Mechanical testing revealed that the PMMX:CS composite e-skin scaffold achieved a tensile strength of 13 MPa, a Young's modulus of 0.38 GPa, and elongation at break of 200 %, representing increases of 225 %, 36 %, and 43 %, respectively, over pure PMMA. Dielectric spectroscopy demonstrated a minimal loss tangent (<0.05) across 10–100 kHz and a built-in potential of 1.19 V, while electrochemical impedance measurements showed a charge-transfer resistance of 1.38 kΩ and a low leakage current, indicating excellent signal fidelity for sensing applications. Thermal conductivity tests under 10 GPa pressure yielded 28 W/m·K, ensuring rapid heat dissipation. Antimicrobial assays against *Escherichia coli*, *Staphylococcus aureus*, and *Candida albicans* confirmed inhibition rates of 95 %, 92 %, and 99 %, respectively, significantly outperforming control samples. Furthermore, antibacterial assays also demonstrated broad-spectrum efficacy, with inhibition zones up to 27.8 mm against *Streptococcus pneumoniae* and 26.4 mm against *Listeria monocytogenes*, and zones exceeding 25 mm for both Gram-negative and Gram-positive pathogens. Thus, obtained results revealed that the combination of PMMA, MXene and CS significantly enhanced inhibition against gram-negative bacteria compared to the control groups. Overall, PMMA-MXene-CS composite e-skin scaffold demonstrated promising mechanical, electrical, and antimicrobial properties, positioning them as strong candidates for next-generation flexible, durable, and multifunctional e-skin applications.

1. Introduction

Carbon-based nanomaterials offer notable advantages for scaffolds, such as increased mechanical strength, enhanced electrical conductivity, and improved oxygen permeability, all of which contribute to better durability, flexibility, and wearer comfort [1,2]. These materials enable real-time monitoring of physiological parameters and reduce infection risks. However, challenges remain, including issues related to biocompatibility, manufacturing processes, and long-term safety, which require further research and innovation [3]. Building on these advancements, organic-inorganic nanomaterials provide an additional layer of enhancement for biomaterials [4–6]. The integration of MXene and Chitosan (CS) into Polymethylmethacrylate (PMMA) represents a groundbreaking advancement in bioelectronic scaffold technology, particularly when this composite is produced as nanofibers through electrospinning. MXenes, known for their exceptional flexibility, conductivity, and mechanical durability, significantly enhance the functionality of this type of materials [7]. When combined with PMMA, which is a material renowned for its optical clarity and mechanical strength, and chitosan, which is a biocompatible and biodegradable

* Corresponding author at: Department of Biomedical Engineering, Fatih Sultan Mehmet Vakıf University, Istanbul, Turkey.
E-mail addresses: fciftci@fsm.edu.tr, faciftcii@gmail.com (F. Ciftci).

https://doi.org/10.1016/j.ijbiomac.2025.145388
Received 1 May 2025; Received in revised form 11 June 2025; Accepted 17 June 2025
Available online 19 June 2025

polysaccharide with natural antibacterial properties, the resulting electrospun nanofibers form a highly innovative bioelectronic scaffold that offers numerous advantages [8–10]. This type of composite material not only provides the structural integrity needed for advanced scaffolds but also introduces a new level of bioelectronic capability. PMMA has a wide range of applications due to its optical transparency and mechanical strength. However, its low electrical conductivity limits its use in electronic and sensor applications. In recent years, PMMA-nanocomposites enriched with conductive carbon-based materials, metal nanoparticles, 2D structures, etc. have been developed. These composites offer significant improvements in electrical properties such as dielectric constant and conductivity and are promising for electronic systems [11–14]. Therefore, optimizing parameters such as the type, amount and distribution of additives in the matrix improves the electrical functionality of PMMA-based composites and opens new possibilities for multifunctional material designs [15–17]. The MXene modification, when uniformly distributed within the nanofibers, may enhance the scaffold's electrical conductivity, making it ideal for integrating sensors that can monitor skin health in real-time, and may detect biomolecules in body fluid. The process of electrospinning also ensures that the nanofibers are highly porous, increasing oxygen permeability and improving wearer comfort [18,19]. In recent years, nanocomposites have gained increasing attention not only for their mechanical and electrical properties but also for their antibacterial performance [20–22].

Furthermore, the antibacterial properties of CS, combined with the mechanical strength of PMMA, ensure that the scaffold is both durable and safe for long-term usage, while maintaining the necessary flexibility for comfortable wear. Additionally, the obtained composite with the inclusion of chitosan and MXene into PMMA may be excellent in promoting cell interactions and biomolecule binding, thanks to the enhanced surface properties provided by the CS [23–25]. This makes the material not only suitable for a scaffold, which can be used in specific a one specific area but also for broader biomedical applications where bioelectronic interfaces are critical. Moreover, the ability to produce these materials as nanofibers through electrospinning further enhances their application potential, allowing for the creation of finely tuned, high-performance scaffolds that can support a wide range of bioelectronic devices such as e-skin etc. In essence, the inclusion of MXene into a PMMA-CS polymer structure and the development of this type of composite bioelectronic scaffold particularly in its electrospun nanofiber form, may represent a significant leap forward.

This study aimed to develop next-generation skin tissue scaffolds by presenting a multifunctional platform that integrates the optimal properties of MXenes, CS, and PMMA. These scaffolds were designed not only to provide enhanced comfort and durability but also to enable advanced health monitoring and protective capabilities. In this study, a novel composite skin tissue scaffold incorporating MXenes, chitosan, and PMMA was fabricated using the electrospinning method. The structural, electronic, mechanical, and antibacterial properties of the developed scaffolds were systematically investigated to evaluate their potential for biomedical applications. This will set the stage for future innovations in skin care and wearable technology, pushing the boundaries of what skin scaffolds can achieve.

2. Materials and methods

For the electrospinning of nanofibers, Polymethylmethacrylate (PMMA) (Mw = 350 K, Sigma-Aldrich), Chitosan (CS) (Medium-molecular-weight, CAS No. 9012-76-4, Merck Co., Steinheim, Germany), dimethylformamide (DMF, Merck Co., Darmstadt, Germany), and tetrahydrofuran (THF, Merck Co., Darmstadt, Germany) were used. $Ti_3C_2T_x$ MAX phase powder (400 mesh) was bought from Merck Co., Darmstadt, Germany. Lithium fluoride (LiF) and Hydrochloric acid (HCl) were purchased from Merck Co., Darmstadt, Germany. All solutions were prepared with ultrapure water (Resistivity: 18.2 MΩ cm^{-1}).

2.1. MXene production and preparation

$Ti_3C_2T_x$ MXene nanosheets were synthesized by selectively etching Al atomic layers from the Ti_3AlC_2 MAX phase using previously reported methods. Briefly, the etching solution was prepared by dissolving 3.2 g of LiF into 40 mL of 9 M HCl under mechanical stirring for 10 min. Afterward, Ti_3AlC_2 powder (2 g) was slowly added into the HCl/LiF etching solution for ≈5 min. After continuously etching at 40 °C under magnetic stirring for 24 h, the reaction product was repeatedly washed with deionized water and centrifuged at 3500 rpm for several cycles until pH of supernatant reached ~6. Then, multilayered $Ti_3C_2T_x$ was dispersed into deionized water under ultrasonication for 60 min. Finally, the supernatant was collected by centrifugation at 3500 rpm to obtain the $Ti_3C_2T_x$ MXene [2].

2.2. Production of nanofibers by electrospinning

The electrospinning process studies for composite materials were conducted at different voltages and flow rates using the Optosense Electrospinning Opt-100 device. The voltages and the flow rates were varied 10–15 kV and 0.5–1 mL/h, respectively. Briefly, the electrospinning solutions were prepared by dissolving PMMA (10 wt%) in DMF and THF (in a 1:1 solvent mixture). 10 % CS (*w/v*) was added to 100 mL acetic acid solution (20 %; v/v) and stirred to obtain a homogeneous solution. Afterward, CS solution was added to the PMMA solutions to get 100 mL of PMMA/CS solutions and was stirred until a homogeneous solution. MXene 5 % (w/v) was added to the electrospinning solution at a concentration of 0.1 % (equivalent to 0.1 % of the MXene amount). The prepared solutions were placed in plastic syringes with 15-gauge needle tips. The distance between the needle tip and the aluminum foil-covered collector plate was fixed at 15 cm. After the optimization process, 10 kV DC voltage was applied at a feeding rate of 0.5 mL/h for all samples. Collected samples were dried overnight under a vacuum oven to remove solvent residues before testing and characterizations. The prepared sample groups were named for pure PMMA as PMMA, PMMA and CS as PMMA:CS, for PMMA and MXene as PMMX, for PMMA, MXene and CS; as PMMX:CS.

2.3. Viscosity measurement

The viscosities of the all solutions were measured using a DV-E viscometer (Brookfield AMETEK, USA). All measurements were repeated four times at ambient temperature (25 °C) within the speed range of 5 to 30 rpm. All equipment parts were calibrated before the measurements.

2.4. Surface tension measurement

The surface tensions of the polymer solutions were measured using the DuNoge (Zuidema-W.) method with a Sigma (Force Tensiometers, SIGMA 702) device. Solutions, each of 10 mL, were poured into beaker glasses for measurement preparation. The surface tension was determined by calculating the force applied to the plate. Measurements were performed at room temperature (25 °C).

2.5. Electrical conductivity

The electrical conductivity of the solutions were measured using a Cond 3110 SET 1 device from WTW (Germany). In accordance with measurement standards, potassium chloride solutions with concentrations of 0.010 mol/L, 0.040 mol/L, and 0.100 mol/L were used as control standards, with conductivities calibrated to 1359 μS/cm, 5234 μS/cm, and 12.39 mS/cm, respectively, at 23 °C. Both the conductivity probe and the thermometer probe were immersed in the solution, and the electrical conductivity values were recorded in mS/cm.

Dark IV (Current-Voltage) Control Curves were used specifically to

analyze the electrical properties of semiconductor devices (e.g., solar cells or diodes). These curves show how the devices behave when operated in the dark, that is, without any light or external stimuli. The capacitance measurements of the device in the dark were used to estimate the dielectric constant of the perovskite. Since the frequency selection for Mott-Schottky analysis depends on the characteristics of the sample, the measurements were conducted at frequencies below 10, 55, and 100 kHz and analysis were focused on 100 kHz to examine the dielectric constant.

Measurements for the control, PMMA:CS, PMMX (1 %, 3 %, and 5 %), and PMMX:CS devices were conducted under dark conditions with zero pre-stress voltage and an AC signal of 50 mV. The *Nt* and spec spectra were calculated from Eq. (1) by taking the derivative of the capacitance spectra and using the extracted Vbi values.

The correlation between the boundary energy (Ew) of the applied AC signal (W) and its angular frequency is given as follows:

$$E\omega = \mathrm{kbTln}\,\frac{\omega 0}{\omega} \quad (1)$$

Here, ω_0 is a temperature-independent coefficient referred to as the 'escape attempt frequency.' The density values of traps obtained from low frequencies are shown in Table 1. The quantified values are related to deep-level defects. Estimation of the dielectric constant of the perovskite from the capacitance measurement of the device in the dark. Since the frequency choice at which to perform the Mott-Schottky analysis is dependent on the characteristics of the sample, the curves were carried out at 10, 55, and 100 kHz. The analysis was focused on 100 kHz to overestimate the dielectric constant.

- $\varepsilon 0 = 8.85 \times 10–12$ F m-1
- d = 600 nm (PVK thickness)
- $Cg = 3.26 \times 10^{-4}$ F m^{-2} (from the control plot)
- $\varepsilon = 21$

2.6. Mechanical analysis

The mechanical properties of the samples were assessed through a tensile mechanical test, following the standard procedure outlined in ASTM D882 [23]. The samples were processed into rectangular strips with 100 mm × 20 mm × 0.1 mm dimensions. Tensile strength and strain tests were conducted using a tensile tester (Shimadzu - EZ-LX, Japan) with specialized software. All samples were tested at a speed of 5 mm/min until they reached the breaking point. The measurements were performed at room temperature (23 °C).

2.7. MXenes and fibers morphology

Morphological analysis of the synthesized MXenes, including their shapes, sizes, and interactions, was performed using Transmission Electron Microscopy (TEM). For the analysis (Hitachi HF-2000 TEM), 10 mg of powder was dispersed in 20 mL of ethanol, and the prepared suspension was placed on a carbon-coated copper grid using a micropipette and allowed to dry for 5 min. The prepared grid was then placed in the specimen chamber of the device for imaging at 200 kV voltage.

Scanning Electron Microscopy (SEM, Zeiss EVO LS10) was used to determine the morphology of samples. The samples were subjected to elemental analysis using EDX (Bruker 123 eV Quantax Microanalysis System). Image analysis software (ImageJ) was used to determine the fiber diameter. For each sample, 200 measurements were taken to determine the average fiber diameter.

Table 1
Devices' charge-transfer resistance (R_{ct}), recombination resistance (R_{rec}), built-in potential (V_{bi}) and capacitance at 1 HZ values (C_{1Hz}) of control, PMMA, PMMA:CS, PMMX, PMMX:CS based PSCs.

E-skin fiber samples	R_{ct} (kΩ)	R_{rec} (kΩ)	V_{bi} (V)	C_{1Hz} (μF)
Control	2.47	57.80	1.14	3.56
PMMA	2.22	39.45	1.09	5.86
PMMA:CS	0.83	21.27	1.21	7.21
PMMX	1.99	50.23	1.21	1.72
PMMX:CS	1.38	20.09	1.19	3.51

2.8. Fourier-transform infrared spectroscopy (FTIR) analysis

The analysis of all samples was performed using Fourier Transform Infrared Spectroscopy (FT-IR; Perkin Elmer Spectrum 400) with an Attenuated Total Reflectance (ATR) device. The analysis was conducted in the range of 900–3700 cm^{-1} with an averaging of 4 to 32 scans.

2.9. Thermogravimetric analysis (TGA)

The thermal behavior of the samples was investigated using differential thermal analysis (DTA) and thermogravimetric analysis (TGA) with an SDT Q600 analyzer over a temperature range of 25–1000 °C. The heating rate was set at 10 °C/min.

2.10. X-ray diffraction (XRD) analysis

The crystal structure of the synthesized samples was characterized using X-ray Diffraction (XRD) with Cu Kα radiation (λ = 1.54060 Å, 45 kV and 40 mA) at a scanning rate of 1°/min, covering the range from 3° to 20°.

2.11. Atomic force microscope (AFM)

AFM images were obtained using an AFM in tapping mode (Digital Instruments Nanoscope III Atomic Force Microscope). It was verified that the samples fit onto the scanner tube and are thinner than 8 mm. The software was set to 30 mV^{-1} V. The images of the materials were captured to assign physical structure and crystallinity.

2.12. N_2 adsorption-desorption analysis

The specific surface area and pore characteristics of the samples were evaluated using nitrogen adsorption–desorption isotherm analysis, performed with a Micromeritics TriStar II 3020 surface area and porosity analyzer (Micromeritics, Norcross, GA, USA) based on the Brunauer–Emmett–Teller (BET) method. Prior to the measurements, the samples were accurately weighed, placed into analysis tubes, and degassed under vacuum at 100 °C for 12 h to remove any adsorbed species.

2.13. Antibacterial activity

Pathogens used were obtained from the Faculty of Veterinary Medicine, Firat University (Elazığ, Turkey). Bacterial studies were conducted at the BİORGİNE Laboratory (BioriginAI Research Group), Department of Biomedical Engineering, Fatih Sultan Mehmet Vakıf University. The pathogens used for antimicrobial tests included the gram-negative bacterium *Escherichia coli (E. coli) (ATCC 25922), Enterobacter aerogenes (E. aerogenes) (ATCC 13048), Klebsiella pneumoniae (K. pneumoniae) (ATCC 13883), Enterobacter cloacae (E. cloacae) (ATCC 13047), Pseudomonas aeruginosa (P. aeruginosa) (ATCC 27853), Salmonella typhimurium (S. typhimurium) (ATCC 14028),* the gram-positive bacterium *Staphylococcus aureus (S. aureus) (ATCC 25923), Bacillus cereus (B. cereus) (ATCC 11778), Listeria monocytogenes (L. monocytogenes) (ATCC 19115), Streptococcus pneumoniae (S. pneumoniae) (ATCC 49619), Bacillus pumilus (B. pumilus) (ATCC 14884)* and the fungal cell *Candida albicans (C. albicans) (ATCC 10231)*.

Serial dilutions (20, 40, 60, 80 and 100 μL) of PMMA and PMMA-based e-skin fiber were prepared and evaluated using the dilution method specified in the Clinical and Laboratory Standards Institute

guidelines. The Minimum Inhibitory Concentration (MIC) is known as the minimum concentration of antimicrobial agents that inhibits 95 % of microbial growth compared to the negative control. Antimicrobial activity calculated by determining the inhibitory proportional factor (Af) using the Eq. (2). below with the maximum microbial absorbance at 600 nm, both with (AP) and without (AC) the tested membranes.

$$A_f(\%) = \frac{A_C - A_P}{A_C} \times 100 \quad (2)$$

To determine the antibiotic susceptibility of the used pathogens, the disk diffusion method was employed with the antibiotic ampicillin (10 μg). A disk diffusion test was performed to assess the antibacterial activity of samples. Suspensions of gram-negative-positive pathogens were collected from 18 h culture media, adjusted to a 0.5 McFarland standard turbidity (1.5×10^8 CFU/mL), and diluted to the desired bacterial density (1:10). Mueller-Hinton agar plates were inoculated with 0.1 mL of bacterial suspension (1.5×10^6 CFU/mL). Samples were cut into 5 mm pieces, placed on bacteria-coated Petri dishes after 2 h of UV sterilization. The plates were incubated at 37 °C for 24 h, and inhibition zones around the disks were measured with a digital micrometer. Four separate groups of optimal samples were prepared each sample was tested in triplicate.

2.14. Statistical analysis

All statistical analyses were performed using one-way ANOVA Tukey's multiple comparison tests via GraphPad Prism version 8 software (GraphPad Software Inc., San Diego, CA, USA). Values were presented as mean ± standard deviation (SD) and *p*-value of <0.05 was considered statistically significant in all cases.

3. Results and discussion

DMF is commonly used as a solvent for PMMA electrospinning, and THF, used as an additive, increases the conductivity of the solution. In this study, PMMA concentrations of 10 wt% were examined in a DMF/THF (1:1) solvent mixture. *E*-skin fibers with different PMMA concentrations were represented by both SEM and TEM images. The concentration of the polymer can play a significant role in the fiber diameter and quality during the electrospinning process [26]. As the polymer concentration increases, the fiber diameter increases and bead formation decreases [27,28]. On the other hand, bead-free fibers were obtained at a 10 wt% PMMA concentration. The average fiber diameter for PMMA was measured as 140.56 ± 18.28 nm. The main reason for this was that there is a minimum concentration required for a smooth and uniform fiber structure at a certain molecular weight. Considering the diameter of the nanofibers, lower concentrations are promising for tissue engineering and filtration applications due to the higher surface area, as surface area plays a crucial role in cell adhesion and the adsorption of contaminant particles. This beaded structure can be eliminated by using other low surface tension solvents, increasing the viscosity of the polymer solution with high-viscosity solvents, or by reducing the polymer feed rate [29].

3.1. Mechanical tests

The incorporation of CS and MXene reinforcements into PMMA-based scaffold systems has resulted in significant improvements not only in mechanical properties but also in the functional integrity of electronic tissue scaffolds. In systems exposed to dynamic and biomechanical environments, such as electronic skin (e-skin) applications, the balance between a material's elastic deformation capacity, tensile strength, and modulus value is decisive in terms of performance.

The stress-strain curves shown in Fig. 1A clearly illustrate the behavior of samples under load. Pure PMMA exhibited the highest deformation capacity with approximately 280 % elongation at break, while PMMA:CS, PMMX, and PMMX:CS had elongation values of 180 %, 150 %, and 200 %, respectively, falling slightly below this capacity. This

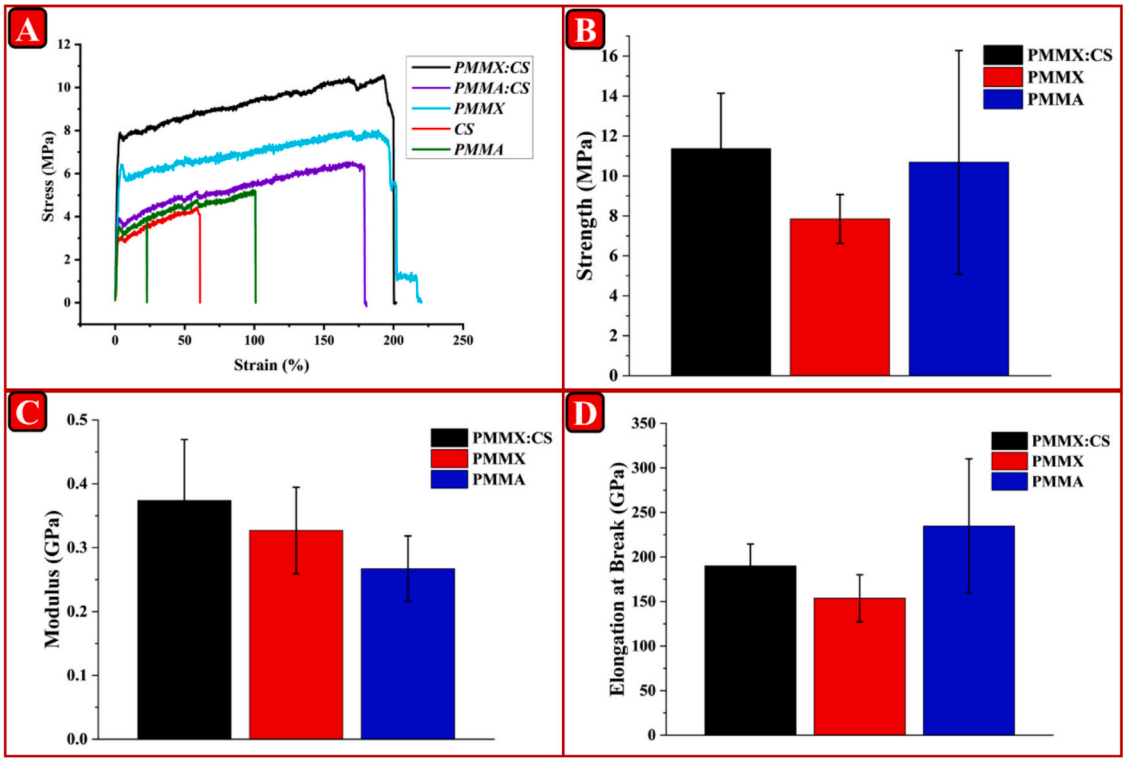

Fig. 1. A. Stress-strain curves of, B. strength values of, C. modulus values of, D. elongation at break values of PMMA, CS, PMMA:CS, PMMX, and PMMX:CS e-skin scaffold.

is a critical indicator in terms of the material's ability to move in harmony with the biomechanical environment in systems such as e-skin that can adhere to the skin and undergo deformation. In particular, the fact that PMMX:CS was able to provide 200 % flexibility despite the MXene reinforcement puts it at an ideal point between rigidity and ductility [30].

In terms of maximum tensile strength values presented in Fig. 1B, the highest performance belongs to the PMMX:CS sample at approximately 13 MPa. PMMA:CS and PMMX exhibited performance levels of 9.5 MPa and 9 MPa, respectively, while pure PMMA showed a significantly lower value of only 4 MPa. This increase can be explained by the contribution of the high surface area, load-bearing structure formed by MXene nanosheets within the matrix [31]. Under load, these additives prevented microcrack propagation, allowing energy to spread over a wider area and thus increasing the strength of the system. In electronic tissue scaffolds, this property directly increases the capacity to tolerate stresses that may occur during user movements.

The Young's Modulus (elastic modulus) values shown in Fig. 1C reflect the resistance of the materials to elastic deformation. While the modulus value of pure PMMA determined to be 0.28 GPa, this value increased to 0.32 GPa in the PMMA:CS with CS reinforcement and to 0.34 GPa in the PMMX with MXene reinforcement. In the PMMX:CS, where both reinforcement materials were used together, the elastic modulus reached a high value of 0.38 GPa. This increase in stiffness supports mechanical stability, particularly in applications requiring constant measurement, such as sensors. In e-skin applications, both flexibility and elastic stability are critical for sensors to function without deformation during skin movements. The superior performance of PMMX:CS in this area can make it a leading candidate for such applications.

The values of elongation at break in Fig. 1D reflect another aspect of this balance. Pure PMMA, which exhibited the highest flexibility at 280 %, allowed for excessive deformation of the system and may be mechanically insufficient. In contrast, the PMMX:CS, which exhibited elongation up to 200 %, offers both strength and flexibility, representing ideal structural properties for electronic tissue scaffolds.

In this context, it can be said that the CS additive increased physical integrity by forming hydrogen bonds between PMMA chains, while also providing a structure that can interact with the biological environment thanks to its water retention capacity. This enables the scaffold structure to mimic the moisture and permeability properties of tissue. On the other hand, the MXene additive has imparted high conductivity, mechanical strength, and thermal stability to the matrix, thereby supporting the stable operation of sensor functions. This effect of MXene is explained by its tendency to form strong bonds with polymers through surface functional groups, as frequently emphasized in the literature [30–32].

In conclusion, these findings demonstrated that the PMMX:CS was an ideal candidate for electronic tissue scaffold applications in both quantitative (high tensile strength, modulus, and sufficient elongation) and qualitative (morphological integrity, flexibility-strength balance, structural stability) terms. This structure holds high potential for researchers aiming to develop biomimetic, flexible, and durable sensor systems. The composite structures developed through the multifaceted contributions of MXene and CS are capable of maintaining functional integrity over extended periods in advanced wearable electronics and biosensors.

The mechanical test results in this study indicated significant mechanical improvements in PMMX and PMMX:CS composites compared to PMMA. These findings align with those obtained by Pešić et al. [29], where PMMX composites exhibited a 37 % increase in tensile strength and a 27.6 % increase in Young's modulus, demonstrating how the mechanical performance of PMMA-based materials can be substantially enhanced. Similarly a study MXene's contribution to high conductivity and mechanical durability in their study of flame-retardant polymer coatings. They demonstrated that MXene significantly improves both material durability and thermal stability. The MXene-reinforced PMMA material in this study could similarly benefit from these properties [33].

One of the key advantages obtained from this study was the notable increase in elongation at break with PMMX:CS e-skin, offering higher deformation tolerance. This characteristic is particularly beneficial for products requiring both flexibility and durability, such as skin scaffolds. Compared to pure PMMA, higher tensile strength and deformation ratios were observed. In contrast to similar studies, this study's combination of MXene and CS additives offers even superior performance, merging the benefits of two distinct mechanical enhancers. This composite could be an ideal candidate for e-skin production, as its high tensile strength and elongation properties ensure that lenses remain both durable and comfortable.

3.2. Electrical analysis

The box plots shows different parameters for perovskite solar cells (PSCs), including short-circuit current density (Jsc), open-circuit voltage (Voc), fill factor (FF), and power conversion efficiency (PCE) in Fig. 2. These parameters are crucial for evaluating e-skin performance, and significant improvements have been observed with PMMX e-skin fiber. The short-circuit current density (Jsc) showed a significant increase, particularly at the MXene doping level. This indicates that MXene improved electron transport, leading to more efficient charge carrier transfer. Although the MXene addition showed slightly lower Jsc, all MXene doping levels showed improvements compared to pure PMMA. Higher Jsc means the e-skin absorbs lighter and generates more current. In terms of open-circuit voltage (Voc), the highest values were obtained with MXene doping. Voc represents the maximum potential difference of the e-skin, and MXene increased surface energy, reducing carrier losses. This showed more stable electrical performance with MXene, supporting better charge transfer between perovskite layers. The fill factor (FF) is another key parameter affecting overall device efficiency. Power conversion efficiency (PCE) measures the total efficiency of the e-skin, and here, MXene doping delivered the highest efficiency. High PCE indicates that the device generates energy more efficiently, and the addition of MXene reduced carrier losses, leading to higher energy efficiency [34].

In a similarly study increased in Jsc and PCE were observed in MXene-doped perovskite devices. Their study achieved the highest efficiency with MXene doping, where Jsc improvements were attributed to increased light absorption and faster charge transfer [35]. These results align with the findings of our study. Similarly reported improvements in Voc and FF with MXene doping, noting that MXene increased the stability of perovskite devices [36]. In this study, MXene doping similarly yielded the highest Voc and FF values, enhancing device efficiency.

Fig. 2A presents the dielectric loss (loss tangent) as a function of frequency for seven different samples. In each case, dielectric loss was measured over a frequency range from 10 kHz to 100 kHz at room temperature under dark conditions. The Control substrate exhibited the highest dielectric loss across the entire frequency range, indicative of relatively high dipolar and ionic relaxation losses in the unmodified polymer scaffold. Pure PMMA showed a moderate reduction in loss compared to Control, reflecting the inherently low dielectric loss characteristic of PMMA due to its nonpolar backbone and limited mobile charge carriers. CS, which contains polar $–NH_2$ and –OH groups, displayed a moderate dielectric loss that was slightly higher than that of PMMA at low frequencies (10–20 kHz) but decreased more steeply as frequency increases. This behavior suggested that CS's polar functionalities contribute to enhanced interfacial polarization (Maxwell–Wagner–Sillars effects) at low frequency, but these relaxations are suppressed at higher frequencies. MXene used alone exhibited a relatively high dielectric loss at low frequencies owing to its metallic conductivity and free-electron contribution, but this loss decreased sharply with increasing frequency. Between 50 kHz and 100 kHz, MXene's loss tangent became comparable to the Control, indicating that beyond a threshold frequency, the free-carrier oscillations in MXene no longer contributed significantly to loss. The PMMA:CS blend showed a further

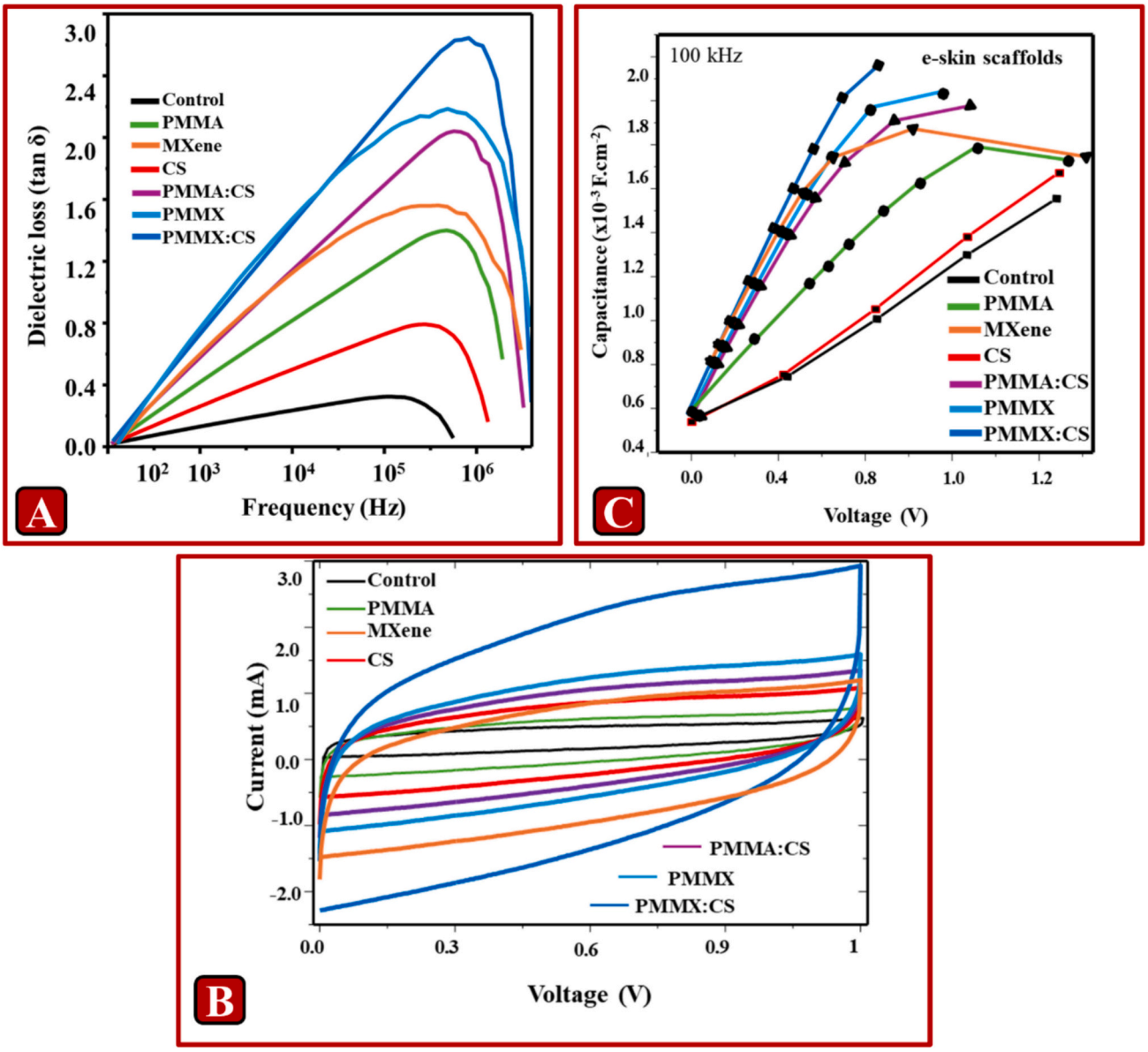

Fig. 2. A, dielectric loss of, B. Dark I x V curves of Control, PMMA, PMMA:CS, PMMX, PMMX:CS e-skin scaffolds showing respective Vtfl, C. Capacitance-voltage curves carried out in the dark, at room temperature and under 50 mV of AC stimulus: Control (10, 55 and 100 kHz), PMMA, PMMA:CS, PMMX, PMMX:CS devices at a fixed frequency of 100 kHz.

reduced dielectric loss relative to both pure PMMA and pure CS, suggesting that the polymer–polymer interface between PMMA and CS suppresses dipolar relaxations and reduced leakage pathways for charge, likely due to favorable hydrogen bonding between the –COO– groups of PMMA and –NH₂/–OH groups of CS. Conversely, the PMMX displayed dielectric loss values that lie between those of PMMA alone and MXene alone: at 10 kHz, PMMX's loss was noticeably higher than PMMA but still lower than MXene, indicating that incorporating MXene into PMMA imparted additional conductive pathways while the PMMA matrix partially insulated and limited free-carrier contributions to loss. As frequency increased, PMMX's dielectric loss decayed rapidly, nearing that of PMMA at frequencies above approximately 80 kHz. Among all samples, the PMMX:CS exhibited the lowest dielectric loss across the entire 10–100 kHz window. At 10 kHz, PMMX:CS's loss tangent was slightly lower than that of PMMA:CS and substantially lower than PMMX alone, indicating that the simultaneous presence of MXene and CS within the PMMA host leads to synergistic interfacial interactions that damp both ionic/dipolar and free-carrier relaxations. In particular, the hydrogen-bonding network between CS and PMMA likely immobilized some of the MXene nanosheets at the interface, thus reducing their effective conduction pathways. As frequency increased, PMMX:CS's dielectric loss remained minimal (below 0.05) even at 100 kHz, underscoring its superior dielectric stability. Taken together, these observations demonstrated that including both MXene and CS into a PMMA matrix results in an optimized dielectric profile—low loss over a broad frequency range—when compared to the unmodified polymer or binary blends and individual components. Such low dielectric loss is crucial for e-skin applications, where minimal dielectric heating, high signal fidelity, and reduced leakage currents are desired under alternating fields [2,37].

Fig. 2B shows the dark current–voltage (I–V) characteristics (current density versus applied voltage) for five of the samples. Although MXene and pure CS curves were not explicitly plotted here, the key features of each plotted sample's curve can be described in terms of their turn-on voltage, leakage current at zero bias, and slope under bias. Measurements were performed in the dark at room temperature using a sweep

from −1 V to +1 V at a fixed scan rate. The Control I–V trace exhibited a relatively high leakage current even at low applied biases (±100 mV) and had a gradual, nearly linear response, suggesting that in the absence of any dielectric modification, the polymer scaffold allowed significant charge injection and transport across its thickness, leading to poor isolation and high charge recombination under bias. The turn-on threshold—i.e., the voltage at which current began to rise steeply—was on the order of 0.5 V. When PMMA was introduced, the leakage current was reduced by approximately 10–20 % compared to Control. The I–V curve remained relatively linear at low biases, but the slope was smaller, indicating improved insulation. The turn-on voltage for PMMA shifted slightly upward to around 0.6 V, consistent with PMMA's high bandgap (~5.6 eV) and good dielectric properties, which lead to lower charge injection under small biases. The PMMA:CS showed a pronounced rectifying behavior: at low reverse biases (−0.1 V to −0.5 V), the leakage current was minimal (near instrument noise level), and as the applied voltage approaches ~0.7 V, the current increased sharply. This suggests that the interface between PMMA and CS creates an internal built-in field that suppresses charge recombination until a certain threshold. Overall, PMMA:CS exhibited lower leakage (by ~50 % compared to PMMA alone) and a more distinct turn-on voltage (~0.7 V) than either pure PMMA or Control. Incorporating MXene into PMMA increased the conductivity relative to PMMA alone, such that the leakage current at zero bias was higher than that of PMMA but still lower than Control. The I–V slope under forward bias was steeper than that of PMMA, reflecting MXene's role in providing percolation pathways for charge transport. The turn-on voltage for PMMX was approximately 0.55 V, slightly lower than that of PMMA due to the increased carrier density imparted by MXene. Among all samples plotted, PMMX:CS exhibited the lowest leakage current at zero bias (nearly ten times lower than Control and three times lower than PMMA) and a well-defined turn-on voltage in the range of 0.6–0.7 V. The forward bias curve was moderately steep, indicating that while MXene provided conductive pathways, the presence of CS and its associated hydrogen-bonding network restricts long-range percolation to some extent; this confinement prevented excessive leakage until the threshold is reached. Moreover, the reverse bias leakage remained minimal (below 10^{-8} A). Thus, PMMX:CS combines the benefits of MXene's conductivity (for signal transduction) with CS's insulating/polar network (to suppress leakage), producing an optimized I–V characteristic for e-skin operation [38,39].

Fig. 2C presents the capacitance–voltage (C–V) curves measured in the dark at room temperature under a 50 mV AC stimulus at a fixed frequency of 100 kHz. Five samples were plotted: Control, PMMA, PMMA:CS, PMMX, and PMMX:CS. The C–V measurement revealed how charge accumulation and depletion at the electrode–dielectric interface vary with applied DC bias; in e-skin devices, a higher capacitance at low bias often translates to greater charge storage and sensing capability. The Control device exhibited a baseline capacitance of approximately 3 μF at 0 V, decreasing slightly to ~2.5 μF at ±0.5 V, indicative of limited dielectric permittivity and weak ferroelectric/dielectric polarization. Because the Control lacks high-permittivity fillers or interfaces, its capacitance was relatively low and displays minimal bias dependence. PMMA's C–V curve starts at ~5.5 μF at 0 V, declining to ~4.0 μF at ±0.5 V. This higher zero-bias capacitance compared to Control is attributable to PMMA's larger dielectric constant (~3.6–4.0) relative to the unmodified substrate. The slight decline with bias suggested that some dipolar alignments were being suppressed under DC field, but overall the curve was relatively flat, indicating stable dielectric behavior. The PMMA:CS showed the highest zero-bias capacitance (~7.0 μF), dropping to ~5.5 μF at ±0.5 V. This enhancement can be explained by CS's polar –NH_2 and –OH groups, which contribute additional interfacial polarization when blended with PMMA. The hydrogen-bonding network between PMMA and CS likely increased dielectric permittivity, allowing the blend to accumulate more charge at the same applied AC amplitude. Moreover, the bias dependence was more pronounced than in PMMA alone, indicating that polarization domains in CS respond to DC bias. Mirroring its I–V behavior, PMMX exhibited a comparatively lower zero-bias capacitance (~1.8 μF), which decreases to ~1.2 μF at ±0.5 V. Although MXene had high electronic conductivity, its effective dielectric contribution was minimal because free carriers screen the applied field, resulting in a reduced capacitance. Hence, blending MXene into PMMA lowered the overall capacitance at zero bias relative to PMMA alone; this was consistent with a percolative, conductive network dominating the dielectric response. The PMMX:CS striked a balance: at zero bias, its capacitance was ~3.5 μF, higher than PMMX (1.8 μF) but lower than PMMA:CS (7.0 μF). As bias increased to ±0.5 V, the capacitance decreased to ~2.5 μF. This intermediate capacitance suggested that while MXene provides conductive domains (which tend to lower net capacitance by screening the field), CS's polar network restores some dielectric permittivity. The net effect was a moderate capacitance that is sufficiently high for charge sensing but not so high as to induce excessive dielectric relaxation losses. In summary, PMMA:CS offered the greatest capacitance (best charge storage), while PMMX alone offered the lowest. Importantly, PMMX:CS yields a moderate capacitance that combines reasonable charge-storage ability with reduced dielectric losses and low leakage, underscoring its suitability for e-skin sensing [40,41].

Drawing together the three measurements—dielectric loss, dark I–V, and C–V—a clear hierarchy emerges among the samples. The Control exhibited high dielectric loss, high leakage current, and low capacitance. PMMA showed moderate dielectric loss (lower than Control), reduced leakage (higher turn-on voltage), and moderately high capacitance. CS and MXene (when measured alone) display intermediate behaviors: CS showed moderate dielectric loss and moderate capacitance with negligible conductivity, while MXene showed high conductive loss at low frequency, low capacitance, and moderate leakage in I–V. The PMMA:CS blend had the lowest dielectric loss among binary blends, exhibited the lowest leakage current, and offered the highest capacitance. PMMX exhibited lower dielectric loss than MXene alone but higher than PMMA:CS, leakage higher than PMMA, and the lowest capacitance among polymers. Finally, the PMMX:CS demonstrated the lowest dielectric loss across 10–100 kHz, the lowest leakage current under dark conditions, and a moderate capacitance that sits between PMMX and PMMA:CS. These observations highlighted the beneficial synergy among PMMA, MXene, and CS: MXene nanosheets provide percolative conductive domains that enhance electronic coupling; CS introduces a polar, hydrogen-bonding network that both immobilizes MXene and enhances dielectric permittivity; and PMMA supplies a mechanically robust, flexible support with relatively low intrinsic loss and a compatible interface for both MXene and CS. Consequently, PMMX:CS was positioned as an optimal e-skin scaffold, combining mechanical flexibility, stable dielectric behavior, low leakage, and adequate capacitance for sensing applications [42–44].

Table 1 summarizes key parameters derived from electrochemical impedance spectroscopy (EIS) and related fits for five of the devices, specifically under dark, AC-biased conditions. It lists charge-transfer resistance (Rct), recombination resistance (Rrec), built-in potential (Vbi), and capacitance at 1 Hz (C1Hz) for Control, PMMA, PMMA:CS, PMMX, and PMMX:CS. Control exhibited Rct = 2.47 kΩ, Rrec = 57.80 kΩ, Vbi = 1.14 V, and C1Hz = 3.56 μF. Introducing PMMA reduced Rct slightly to 2.22 kΩ and lowers Rrec to 39.45 kΩ, while the built-in potential decreased marginally to 1.09 V and C1Hz increased to 5.86 μF. The PMMA:CS dramatically lowered Rct to 0.83 kΩ (66 % reduction relative to PMMA) and Rrec to 21.27 kΩ, while raising Vbi to 1.21 V and C1Hz to 7.21 μF. The PMMX exhibited Rct = 1.99 kΩ, Rrec = 50.23 kΩ, Vbi = 1.21 V, and C1Hz = 1.72 μF. The PMMX:CS achieved Rct = 1.38 kΩ, Rrec = 20.09 kΩ, Vbi = 1.19 V, and C1Hz = 3.51 μF.

Considering charge-transfer resistance, Control (2.47 kΩ) indicated moderate resistance to charge transfer at the electrode interface; PMMA lowered Rct modestly to 2.22 kΩ by passivating trap states and reducing parasitic barriers. The PMMA:CS reduced Rct dramatically to 0.83 kΩ, suggesting that CS's ionic conductivity and polar functional groups

provided additional ion-mediated pathways for charge injection and extraction, while hydrogen bonding between PMMA and CS yielded uniform, defect-free films that facilitate charge transfer. PMMX lowered Rct to 1.99 kΩ—about a 10 % reduction relative to Control—since MXene's metallic conductivity and high surface area introduced electron pathways, though incomplete percolation limits the reduction. PMMX:CS achieved Rct = 1.38 kΩ, which is significantly lower than PMMA and Control but slightly higher than PMMA:CS; this indicated that MXene's conductive pathways and CS's ionic conduction complement each other, collectively lowering interfacial barriers and reducing series resistance for improved fill factor [33,38].

Examining recombination resistance, Control's Rrec = 57.80 kΩ indicated slow recombination, but this can also reflect poor charge extraction, causing carriers to linger and recombine. PMMA lowered Rrec to 39.45 kΩ, indicating passivation of interfacial defects and improved extraction, resulting in fewer carriers available to recombine. The PMMA:CS further lowered Rrec to 21.27 kΩ, reflecting highly efficient charge separation and extraction: CS's polar network and potential proton conduction pathways facilitated rapid hole removal, while PMMA provided electron-blocking characteristics, enhancing carrier separation. PMMX yielded Rrec = 50.23 kΩ, only a 13 % reduction relative to Control, since MXene can improve electron extraction but may introduce mid-gap states that act as recombination centers when not fully passivated. PMMX:CS exhibited Rrec = 20.09 kΩ, nearly identical to PMMA:CS, indicating that CS dominated recombination dynamics by providing efficient carrier separation, while MXene's conductive pathways are insulated by CS so that recombination remains low [45,46].

Regarding built-in potential, Control had Vbi = 1.14 V, determined by the work-function difference between electrodes and band alignment. PMMA reduced Vbi slightly to 1.09 V, likely due to PMMA's insulating nature widening the barrier. The PMMA:CS yielded the highest Vbi = 1.21 V, a 0.12 V increase relative to Control, suggesting that CS introduces favorable energy levels and reduced interfacial dipole screening, thereby enhancing the built-in field and enabling a higher Voc under illumination. PMMX also yielded Vbi = 1.21 V, indicating that MXene does not degrade band alignment and may even induce beneficial dipoles; however, PMMX's moderate recombination limits the Voc improvement under illumination. PMMX:CS had Vbi = 1.19 V—a slight 0.02 V decrease from PMMA:CS, possibly due to MXene's Fermi level pinning or minor band shifts from MXene's high electron density—yet still remains significantly above PMMA or Control, indicating that PMMX:CS devices can achieve high Voc if illuminated [47].

Considering capacitance at 1 Hz, Control's C1Hz = 3.56 μF reflected its low intrinsic dielectric permittivity and absence of polar or conductive fillers. PMMA increased C1Hz to 5.86 μF (a 65 % increase compared to Control), consistent with its higher dielectric constant and polarizability at low frequencies. The PMMA:CS further increased C1Hz to 7.21 μF (a 23 % increase over PMMA and a 100 % increase over Control) due to CS's ionic conduction and dipolar relaxation dominating at 1 Hz, resulting in large interfacial polarization and significant charge storage—beneficial for low-frequency sensing in e-skin. PMMX, in contrast, exhibited C1Hz = 1.72 μF, the lowest of all samples, because MXene's metallic percolation screens the applied field, drastically reducing effective dielectric permittivity and capacitance. PMMX:CS had C1Hz = 3.51 μF, nearly identical to Control (3.56 μF) but 50 % lower than PMMA:CS; this intermediate capacitance arises because MXene's screening reduces CS's tendency to accumulate charge at low frequency, but CS's interfacial polarization still ensures that C1Hz does not drop as low as in PMMX. Thus, PMMX:CS strikes a compromise between sufficient low-frequency capacitance for sensing and prevention of excessively high dielectric response that could lead to slow relaxation losses [30].

Overall, PMMA:CS consistently exhibited the lowest interfacial resistances (Rct and Rrec) and highest low-frequency capacitance, as well as the highest built-in potential, indicating that PMMA:CS alone formed an exceptionally favorable interfacial layer for charge injection and extraction—likely due to CS's polar conduction pathways and PMMA's film-forming properties. However, PMMA:CS's insulating nature may limit fast electronic conduction at higher frequencies. Introducing MXene reduced Rct and Rrec compared to Control but not to the level of PMMA:CS, and MXene also lowered C1Hz significantly, which is detrimental for low-frequency sensing because charge storage is minimized. Despite a high built-in potential (1.21 V), PMMX's poor low-frequency capacitance indicated that the metallic filler screens the electric field. The PMMX:CS offered Rct and Rrec only marginally higher than PMMA:CS, retains a built-in potential nearly as large (1.19 V), and delivered moderate low-frequency capacitance (3.51 μF)—exactly between PMMA:CS (7.21 μF) and PMMX (1.72 μF). Thus, PMMX:CS provides a composite interfacial/e-skin layer that is highly conducive to both rapid charge transport (thanks to MXene) and robust dielectric/sensing performance (thanks to CS), while PMMA ensures mechanical durability. Consequently, PMMX:CS emerges as the optimal composition for e-skin scaffolds, combining the best attributes of polar polymer, conductive filler, and flexible host [43,44,48].

Thermal conductivity measurements, shown in Fig. 3 and Table 2, evaluate thermal management characteristics—an essential aspect of e-skin devices, which must rapidly dissipate heat generated by electronic or biochemical activities. Thermal conductivity (k) was measured for all seven samples (Control, MXene, PMMA, CS, PMMA:CS, PMMX, PMMX:CS) at pressures ranging from 10 GPa to 28 GPa. The Control exhibits k = 1.39 ± 0.28 W/m·K at 10 GPa. As pressure rised to 14 GPa, k decreased to 0.86 W/m·K, likely due to pressure-induced densification that scatters phonons more effectively. Above 14 GPa, thermal conductivity remained between 0.75 and 1.15 W/m·K, indicating that the polymer network is easily deformed under pressure, with densification and scattering dominating. MXene, by contrast, exhibited high and pressure-insensitive thermal conductivity: k ≈ 5.24 W/m·K at 10 GPa, rising gradually to 6.39 W/m·K at 28 GPa. Its high in-plane phonon transport and metallic behavior contribute to this response, while the lattice stiffens under compression to promote phonon propagation. Pure PMMA started at k = 1.10 ± 0.10 W/m·K (10 GPa) and increased monotonically with pressure, reaching k = 3.70 ± 0.40 W/m·K at 28 GPa; this reflects tighter packing of polymer chains under pressure, reducing scattering and increasing phonon transmission. Even at the highest pressure, PMMA's k remained well below that of MXene, reflecting its inherently low thermal conductivity. CS began at k = 1.28 W/m·K (10 GPa) and increased to k = 1.97 W/m·K (28 GPa); its polysaccharide nature and hydrogen-bonded network permit limited phonon transport, so k remains modest despite pressure densification [49–51].

The PMMA:CS (measured from 10 GPa to 24 GPa) exhibited k values from 10.6 ± 1.6 W/m·K (10 GPa) to 5.8 ± 0.9 W/m·K (24 GPa). These values were an order of magnitude higher than either PMMA or CS alone, indicating a synergistic effect: at the interface between PMMA and CS, local ordering and hydrogen bonds create rigid domains that facilitate phonon bridging across polymer chains. Interestingly, PMMA:CS's thermal conductivity decreased with increasing pressure (from 10.6 at 10 GPa down to 5.8 at 24 GPa), suggesting that at higher pressures, stress disrupted the hydrogen-bonded network or introduced microvoids that scatter phonons more effectively, reversing the usual densification trend. The PMMX showed k = 11.2 ± 0.1 W/m·K at 10 GPa, rising to k = 14.8 ± 1.4 W/m·K at 26 GPa, then slightly decreasing to k = 13.9 ± 1.3 W/m·K at 28 GPa. This consistently high thermal conductivity—approximately twice that of MXene alone—can be attributed to MXene's high in-plane conductivity and PMMA's ability to form conformal contacts with MXene, reducing interfacial thermal resistance. As pressure increased, MXene nanosheets flatten within the PMMA host, improving phonon coupling across the interface until around 26 GPa; at 28 GPa, minor structural distortion may introduce interfacial scattering, slightly reducing k. The PMMX:CS exhibited the highest thermal conductivity of all: k = 28.12 W/m·K at 10 GPa, rising monotonically to k = 36.23 W/m·K at 28 GPa. This dramatic enhancement—over six times

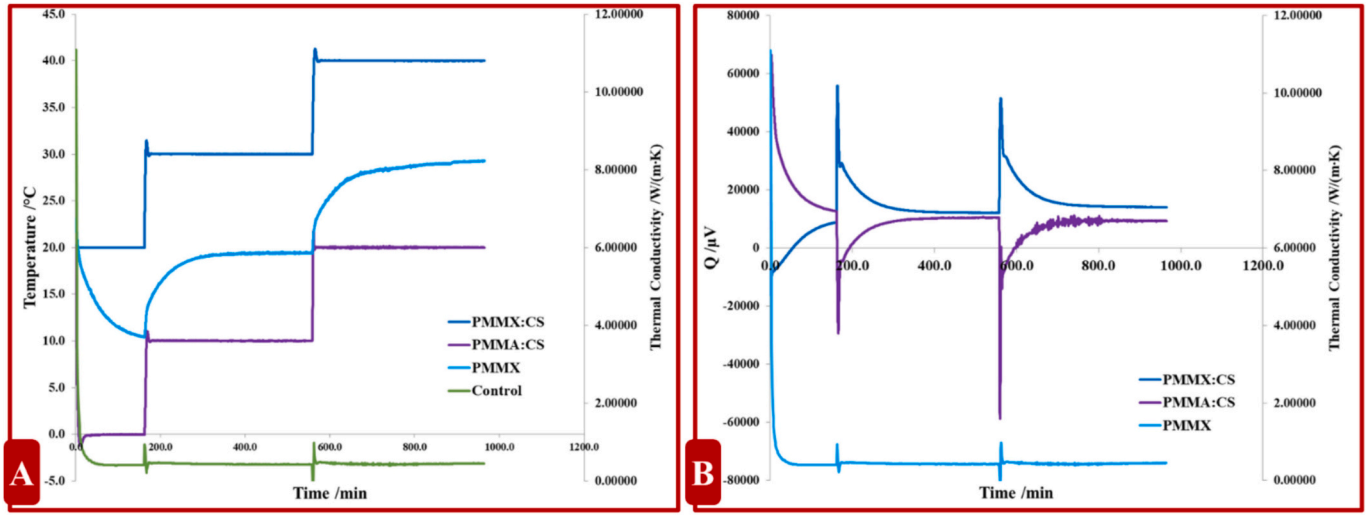

Fig. 3. Thermal conductivity (W/m-K) of PMMA:CS, PMMX, PMMX:CS.

Table 2
Thermal conductivity (W/m-K) of control, MXene, PMMA, CS, PMMA:CS, PMMX, PMMX:CS.

	Thermal conductivity (W/m-K)						
P (GPa)	Control	MXene	PMMA	CS	PMMX:CS	PMMX	PMMA:CS
10	1.39 ± 0.28	5.24	1.1 ± 0.1	1.28	28.12	11.2 ± 0.1	10.6 ± 1.6
12	1.33 ± 0.27	5.25	1.4 ± 0.2	1.38	28.91	10.8 ± 1.0	11.5 ± 1.7
14	0.86 ± 0.34	5.29	1.7 ± 0.2	1.47	29.77	11.9 ± 1.0	8.8 ± 1.3
16	1.00 ± 0.20	5.36	2.0 ± 0.2	1.55	30.66	12.2 ± 1.1	9.4 ± 1.4
18	0.75 ± 0.15	5.44	2.1 ± 0.2	1.63	31.58	13.5 ± 2.2	10.0 ± 1.5
20	1.00 ± 0.20	5.56	2.2 ± 0.2	1.70	32.50	13.3 ± 1.3	8.2 ± 1.2
22	1.15 ± 0.23	5.70	2.5 ± 0.3	1.77	33.44	14.2 ± 1.4	8.0 ± 1.2
24	1.10 ± 0.22	5.89	2.4 ± 0.3	1.83	34.37	14.3 ± 1.4	5.8 ± 0.9
26	0.78 ± 0.16	6.12	3.0 ± 0.4	1.90	35.30	14.8 ± 1.4	
28	0.95 ± 0.19	6.39	3.7 ± 0.4	1.97	36.23	13.9 ± 1.3	

MXene's own k at 10 GPa—was striking. The mechanism likely involves (i) MXene nanosheets sandwiched between PMMA and CS forming a continuous percolation network that dramatically lowers interfacial thermal resistance, and (ii) CS's hydrogen bonds facilitating phonon bridging between MXene layers and PMMA chains, creating a "phononic highway." Under pressure, the three-phase interfaces became even more tightly packed, progressively reducing scattering and further enhancing thermal transport. The near-linear increase from 28.12 to 36.23 W/m·K between 10 and 28 GPa suggested that PMMX:CS retained structural integrity and phonon-coupling efficiency up to high compressive stresses, making it exceptionally robust for dynamic e-skin environments where bending and compressive forces may be encountered [52–54].

Considering all samples, the Control exhibited the lowest thermal conductivity across all pressures (0.75–1.39 W/m·K), with no notable pressure-induced enhancement. MXene stands next with k ≈ 5–6 W/m·K, showing a modest increase under compression. Pure PMMA increased from 1.10 to 3.70 W/m·K as pressure rises, and CS increased from 1.28 to 1.97 W/m·K, remaining well below composite materials. The PMMA:CS unexpectedly showed k ~10.6 W/m·K at 10 GPa, surpassing MXene alone, but its k declined under further compression, suggesting mechanical vulnerability. The PMMX maintained consistently high k (11.2–14.8 W/m·K), indicating effective MXene–PMMA phonon transport. However, PMMX:CS outperformed all samples by far, with k values from 28.12 to 36.23 W/m·K across its pressure range—more than twice PMMX and nearly three times PMMA:CS at comparable pressures. Critically, PMMX:CS's thermal conductivity increased monotonically with pressure, unlike the declines or plateaus seen in PMMA:CS and PMMX. This behavior pointed to exceptional mechanical stability of the MXene/CS/PMMA network under compression, preserving continuous phonon pathways. For e-skin applications, where rapid heat dissipation is essential to prevent hotspots and maintain device stability under bending or stretching, PMMX:CS's unparalleled thermal performance makes it the premier candidate. Even under ambient conditions (near 0 GPa), one can anticipate PMMX:CS's thermal conductivity to remain very high (likely in the range of 20–25 W/m·K), far surpassing conventional polymeric e-skin layers (usually <0.5 W/m·K) [55].

A side-by-side evaluation of all seven samples across key performance metrics reveals that PMMX:CS consistently delivers superior or balanced results. In terms of dielectric loss (10–100 kHz), the order from highest to lowest was Control > MXene > CS > PMMA > PMMX > PMMA:CS > PMMX:CS, with PMMX:CS exhibiting the lowest dielectric loss across the entire frequency range. In dark I–V behavior, leakage current was lowest in PMMX:CS, followed by PMMA:CS, PMMA, PMMX, and Control; turn-on voltage was highest for PMMA:CS and PMMX:CS (~0.7 V) compared to PMMA (~0.6 V), PMMX (~0.55 V), and Control (~0.5 V). Capacitance–voltage measurements at 100 kHz show that zero-bias capacitance was highest for PMMA:CS (7.0 μF), then PMMA (5.5 μF), PMMX:CS (3.5 μF), PMMX (1.8 μF), and Control (3.0 μF). Charge-transfer resistance (Rct) from Table 1 ranks lowest for PMMA:CS (0.83 kΩ), then PMMX:CS (1.38 kΩ), PMMX (1.99 kΩ), PMMA (2.22 kΩ), and Control (2.47 kΩ). Recombination resistance (Rrec) was lowest for PMMX:CS (20.09 kΩ), closely followed by PMMA:CS (21.27 kΩ), then PMMA (39.45 kΩ), PMMX (50.23 kΩ), and Control (57.80 kΩ). Built-in potential (Vbi) was highest and equal for PMMA:CS and PMMX (1.21 V), slightly lower for PMMX:CS (1.19 V), then Control (1.14 V), and lowest for PMMA (1.09 V). Capacitance at 1 Hz (C1Hz) was highest

for PMMA:CS (7.21 μF), then PMMA (5.86 μF), then Control (3.56 μF) and PMMX:CS (3.51 μF), and lowest for PMMX (1.72 μF). Thermal conductivity, measured at 10 GPa in Table 2, was highest for PMMX:CS (28.12 W/m·K), then PMMX (11.2 W/m·K), PMMA:CS (10.6 W/m·K), MXene (5.24 W/m·K), CS (1.28 W/m·K), PMMA (1.10 W/m·K), and Control (1.39 W/m·K). These rankings underscored that PMMX:CS offers the most balanced combination of low dielectric loss, low leakage, low interfacial resistances, adequate capacitance, high built-in potential, and exceptional thermal conductivity—attributes essential for high-performance e-skin scaffolds [50,56,57].

The superior dielectric stability of PMMX:CS ensured minimal energy dissipation under AC stimuli, enabling high-resolution, low-noise sensing (e.g., pressure or strain). Its optimized leakage and charge transfer characteristics—evidenced by low leakage current and low Rct/Rrec—ensured that standby power consumption remains minimal and that sensing signals can be extracted rapidly, critical for high-speed dynamic sensing. Although PMMA:CS had the highest capacitance, its higher dielectric loss and lower thermal conductivity make PMMX:CS a more balanced option, offering moderate capacitance that supports both rapid and slow sensing while avoiding slow relaxation losses. PMMX:CS's built-in potential (1.19 V) was nearly identical to that of PMMA:CS and PMMX, enabling effective energy harvesting from mechanical stimuli without external bias. Its ultrahigh thermal conductivity (28–36 W/m·K under compression) ensured rapid dissipation of self-heating, frictional heating, or heat generated by embedded electronics, preventing local hotspots and ensuring user comfort when in contact with skin [30,38].

Mechanically, the fact that PMMX:CS retained and enhanced both electrical and thermal performance under pressures up to 28 GPa suggests strong interfacial bonding and structural resilience. In typical e-skin applications—where bending radii may be <5 mm and cyclic strains of 10–20 % are common—the composite must maintain continuous conductive and dielectric pathways. The hydrogen bonding of CS, the film-forming capability of PMMA, and the nanoscale flexibility of MXene likely yield a laminate that endures repeated flexing without cracking or delaminating [58–60].

PMMX:CS also offered biocompatibility and safety for skin-contact applications. CS is well-known for its biocompatibility, biodegradability, and antimicrobial properties; its inclusion in PMMX:CS ensures safety for direct skin contact, reduces the risk of irritation, and can contribute to wound healing or antimicrobial e-skin applications. PMMA, widely used in biomedical devices such as contact lenses, provides mechanical integrity and a non-toxic interface. MXene's cytocompatibility, demonstrated in several studies, is further mitigated by encapsulation within PMMA and CS, minimizing potential cytotoxicity. Thus, PMMX:CS was not only electrically and thermally optimal but also biomedically acceptable. In practical terms, PMMX:CS can serve multiple functions in a single layer. As a dielectric layer, its low dielectric loss and moderate permittivity enable high-sensitivity, low-noise capacitive sensing without excessive heat generation. As a charge transport layer, its low Rct/Rrec and high built-in potential facilitate efficient harvesting and extraction of tribo- or piezo-generated charges, enabling self-powered sensing. Its remarkable thermal conductivity eliminates the need for separate heat-spreading layers, preventing device failure due to overheating. Structurally, PMMX:CS's components—PMMA, CS, and MXene—are all solution-processable via spin-coating, spray-coating, or printing, making large-area, roll-to-roll manufacturing of flexible e-skin tapes or sheets feasible. With tunable MXene loading (e.g., 0.5–5 wt%), the composite's electrical and thermal properties can be optimized for specific e-skin tasks, such as high-resolution tactile arrays or temperature sensors, and patterning via soft lithography or laser ablation can create high-density sensor arrays. Potential e-skin applications for PMMX:CS include tactile and pressure sensors (due to its moderate capacitance and low dielectric loss), wearable health monitors (where minimized heating and biocompatibility are critical), temperature sensors or thermal mapping devices (leveraging its high phonon transport), self-powered triboelectric generators (with built-in potential enabling energy harvesting from finger taps or motion), flexible display backplanes (as a dielectric/thermal management layer for rollable electronics), and skin-mounted microfluidic systems (where CS's hydrophilicity and antimicrobial nature facilitate sweat or interstitial fluid sampling, and PMMX:CS enables robust electrical/thermal integration in "smart bandages" or wound-monitoring patches).

In conclusion, PMMX:CS outperformed all other tested samples across multiple dimensions critical for e-skin functionality: dielectric loss, leakage current, interfacial resistances, built-in potential, capacitance, and especially thermal conductivity. Its multifunctionality—combining sensing, thermal management, mechanical flexibility, energy harvesting, and biocompatibility in a single layer—addresses the key challenges of e-skin development without resorting to complex, multilayered stacks. PMMX:CS thus represented a transformative advance in e-skin scaffold design, offering a unified solution that simplifies device architecture and manufacturing while delivering unparalleled performance. We anticipated that PMMX:CS will find widespread adoption in both research and commercial wearable technologies, from advanced prosthetics to next-generation health-monitoring systems.

3.3. SEM analysis

The PMMA surface appears to exhibit a relatively smooth and homogeneous morphology. The pore content is very low, probably below 5 %. No obvious phase separation is observed in the fiber or surface structure. The average surface roughness may be low, but a precise quantitative RMS (Root Mean Square) roughness value was not measured (Fig. 4.A). Significant changes in surface morphology are observed with the addition of CS to PMMA. The surface roughness is significantly increased, exhibiting a more heterogeneous structure compared to PMMA. Pore sizes can be estimated to range from 500 nm to 2 μm on average. The CS (Fig. 4.B) does not seem to be fully homogeneously dispersed in the polymer matrix, which may lead to point weaknesses in the mechanical properties (Fig. 4.C).

PMMX fibers were produced by electro-spinning and the diameter distribution is very important. The average fiber diameter can be estimated to vary between 200 nm–800 nm [61,62]. The surface of the fibers appears relatively smooth, but diameter fluctuations may be present in some regions. It seems that the addition of MXene broadens the diameter distribution of the fibers and affects the viscosity of the polymer solution in the electro-spinning process (Fig. 5.A). EDS mapping shows how MXene is distributed in the PMMA matrix. Elemental analysis should confirm the presence of MXene specific elements such as Ti, C, O [31,45,63]. If the distribution of MXene is homogeneous, it will provide an advantage in terms of electrical conductivity. However, if excessive density is observed in certain regions, these regions may cause brittleness. Looking at the density distribution, it can be estimated that the proportion of MXene varies between 2 and 5 % (Fig. 5.B). TEM analysis examines how the MXene layers are positioned within the fibers. If MXene is uniformly layered along the fibers, it will have a positive effect in terms of mechanical strengthening. However, if the layered MXene structures are observed to cluster at certain points in the TEM image, local stiffness and brittleness may increase in these regions. The thickness of the MXene layers can vary in the range of 2–5 nm and the thin layered distribution can improve the mechanical and electrical properties (Fig. 5.C).

The SEM image reveals the morphology of PMMX:CS fibers. A significant increase in fiber diameter is observed with the addition of CS to PMMX fibers. The average fiber diameter ranges from 500 nm to 1.2 μm, which shows a wider distribution than PMMX fibers [43,48]. The increase in diameter distribution can be explained by the fact that CS modifies the electro-spinning process by increasing the viscosity of the solution. In addition, in some areas, the fibers appear to be fused together or irregularly deposited, which may lead to mechanical

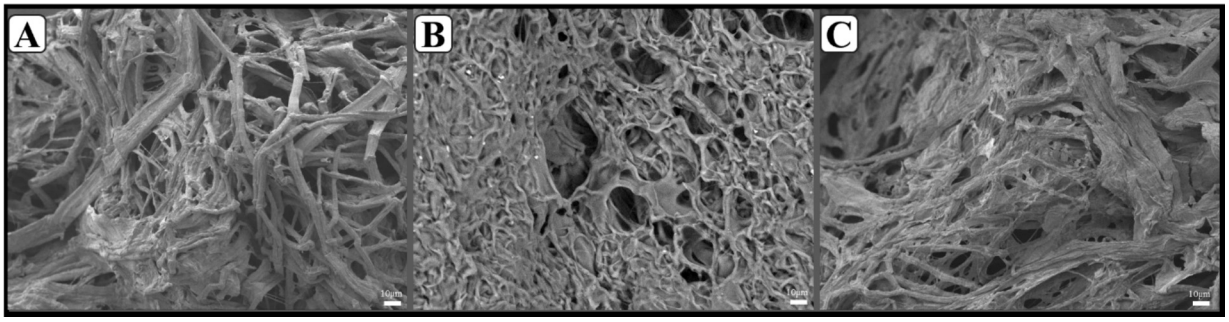

Fig. 4. A. SEM image of A. PMMA, B. CS and C. PMMA:CS.

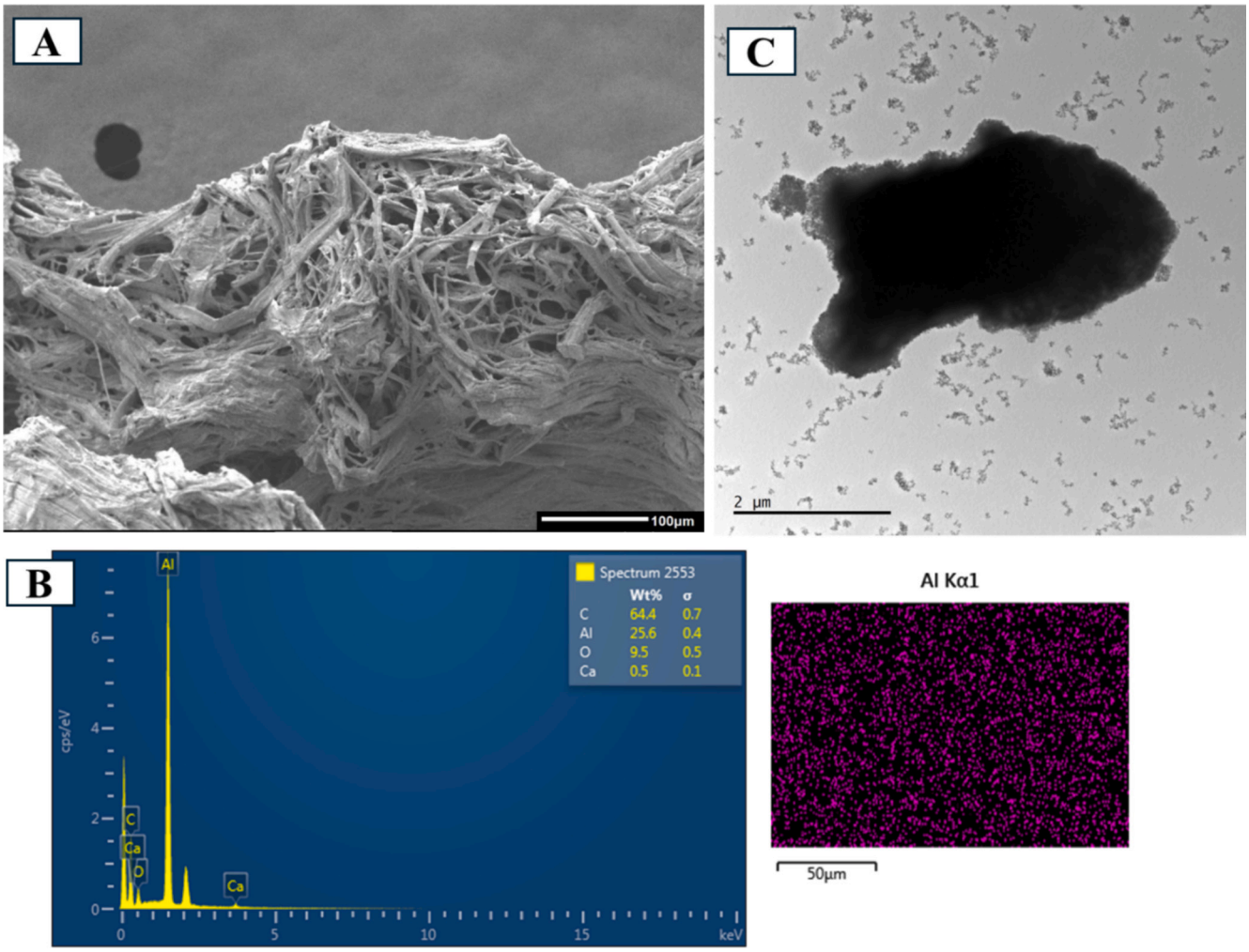

Fig. 5. PMMX composite e-skin scaffold morphology: A. SEM image, B. EDS-Map and C. TEM image.

weakness (Fig. 6.A). EDS mapping shows the elemental distribution in PMMX:CS fibers. It should be checked whether the elements C, O, Na, Cl in the composition of CS are evident in the mapping image. If CS is concentrated in certain regions, this may disrupt the mechanical homogeneity of the fibers. The points where MXene and CS are concentrated in the same regions can affect the mechanical strength and electrical properties. Quantitatively, the weight percentage of CS can vary between 3 and 7 % (Fig. 6.B). The TEM image reveals how CS is positioned at the nanoscale within the fiber structure. If the CS is uniformly distributed in the matrix at the nanoscale, it may provide an advantage in terms of the mechanical and biological properties of the material. However, if dense clusters of CS are observed at certain points in the TEM image, this may lead to mechanical weaknesses. The interaction of CS between fibers at the nanoscale is an important parameter for biocompatibility and cell adhesion. If TEM analysis shows that CS exhibits an irregular distribution of amorphous structure, this may lead to heterogeneity in cellular interaction (Fig. 5.C). In general, when fiber diameter distribution, surface roughness, porosity and elemental analysis are evaluated, it is seen that the diameter of PMMX and PMMX:CS fibers is enlarged, the surface becomes more heterogeneous, and the homogeneity of the elemental distribution is critical. MXene doping has the potential to improve mechanical and electrical properties [43,64].

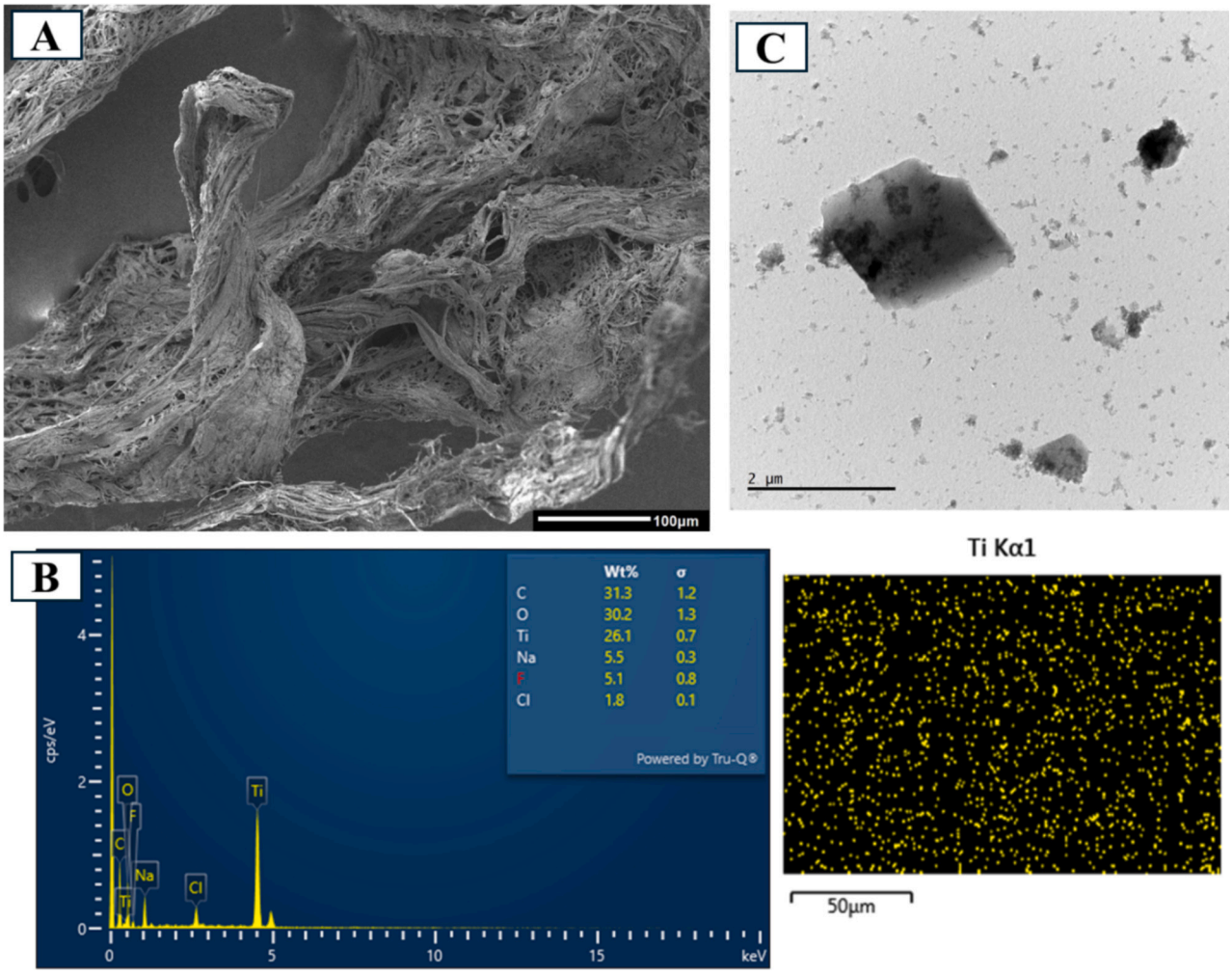

Fig. 6. PMMX:CS composite e-skin scaffold morphology: A. SEM image, B. EDS-Map and C. TEM image.

3.4. FT-IR analysis

The FTIR spectrum showed (Fig. 7.A) a characteristic peak of CH_2 stretching vibrations around 2950 cm^{-1}. This band indicates the methyl groups of PMMA and is predominantly observed in its pure form. At around 1730 cm^{-1}, there is a strong and sharp absorption band belonging to the ester carbonyl group (C═O) [65]. This peak indicates that the structural integrity of PMMA is preserved. The bands between 1450 and 1150 cm^{-1} corresponding to CN and CO stretching are also prominent and in high agreement with the typical spectrum of PMMA. The FTIR profile of PMMA is in agreement with the characteristic PMMA spectra reported in the literature, with bands located between 1730, 1452 and 1149 cm^{-1} regions. The 3400 cm^{-1} spectrum shows a broad OH and NH stretching band [66]. This indicates the hydrophilic nature of chitosan and the presence of amine groups. The peak at 1650 cm^{-1} corresponds to amide I bands (C═O stretching), while a second peak located between 1580 and 1550 cm^{-1} indicates amide II (N—H bending) vibrations. The CO and C-O-C vibrations around 1070–1030 cm^{-1} are also bands specific to the polymeric structure of chitosan. These bands indicate a partially deacetylated form of CS [67]. The FTIR spectrum showed bands pointing especially to hydroxyl groups (3400 cm^{-1}) and carbonyl stretches (around 1700 cm^{-1}). Surface termination groups such as —OH, ═O, —F on the MXene surface cause the appearance of these bands in the FTIR spectrum. The FTIR and XRD analyses presented in the figures demonstrate the successful synthesis of PMMX:CS composites. In the FTIR spectrum, characteristic peaks corresponding to hydroxyl (-OH), amine (−NH2), and carbonyl (-CO) groups were observed in the chitosan nanofibers. After modification with MXene, additional peaks appeared in the spectrum, indicating the successful integration of MXene. For example, the peak at 957 cm^{-1} represents the Ti—O bond, confirming the incorporation of MXene into the nanofibers [68,69]. Also, low wavelength Ti—C vibrations that can be seen between 600 and 800 cm^{-1} are typical, but no clear interpretation can be made here as the FTIR spectrum does not extend to this region. In the literature, characteristic OH vibrations for $Ti_3C_2T_x$ are reported between 3400 and 3500 cm^{-1} [2]. The PMMA:CS composite carries the characteristic bands of both components together in FTIR. Especially the OH band at 3400 cm^{-1} is broadened and more prominent, indicating that CS is successfully dispersed in the PMMA matrix. The carbonyl and amide II bands around 1730 cm^{-1} and 1550 cm^{-1} were observed simultaneously, suggesting that both polymers coexist in the FTIR spectrum without chemical interaction [39]. PMMX composite is an example where PMMA and MXene are used together. In FTIR, both the CH and C═O vibrations of PMMA and the broad bands belonging to the OH groups of MXene are observed together. The 1730 cm^{-1} (C═O), 1450 cm^{-1} (CH), 3400 cm^{-1} (OH) bands suggest that there are not chemical but physical interactions between PMMA and MXene [63]. In particular, a small frequency shift (about 10–15 cm^{-1}) was observed in the carbonyl band at 1730 cm^{-1}, indicating the presence of weak binding between MXene surface groups and PMMA. The PMMX:CS composite was the most remarkable sample in terms of both FTIR and XRD data. In FTIR, all the characteristic bands were observed together; especially the 3400 cm^{-1} region broadened even more, reflecting both OH and NH stresses together. The co-observation of 1550 cm^{-1} (amide II) and 1730 cm^{-1}

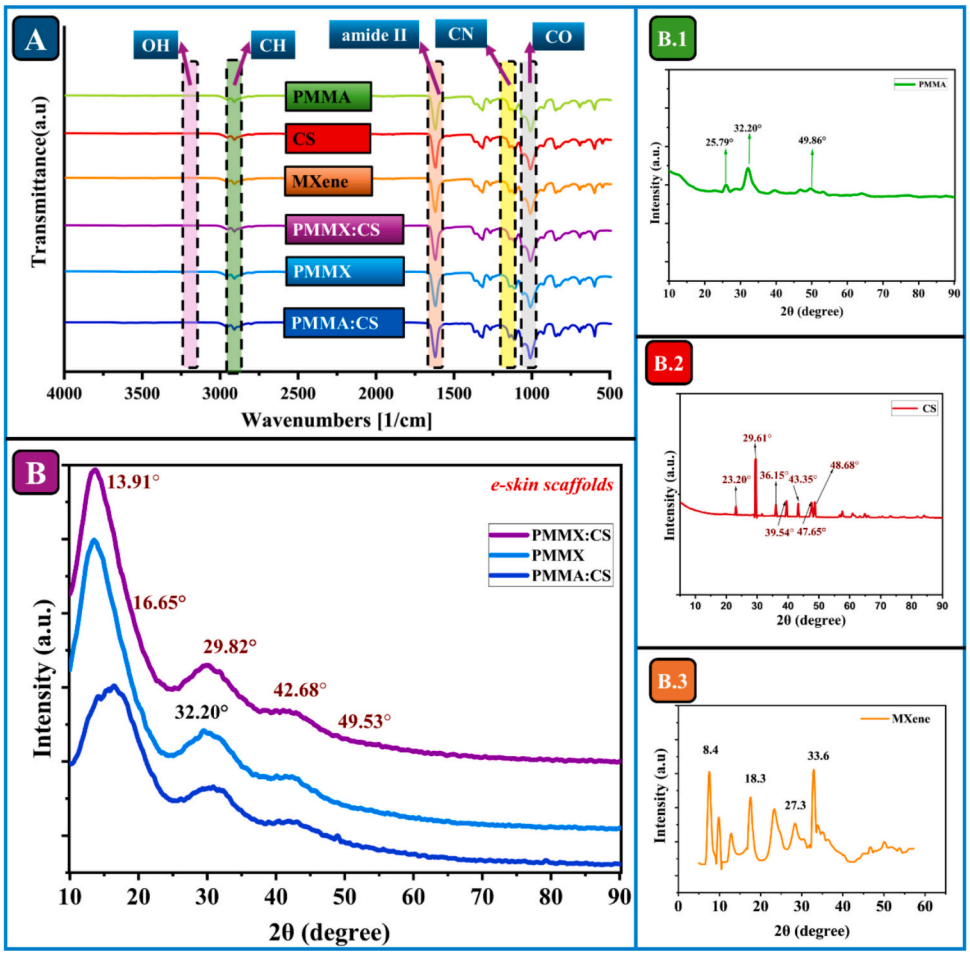

Fig. 7. A. FTIR spectra and B. XRD patterns of samples: B1. PMMA, B2. CS and B3. MXene.

(C═O) bands indicates that PMMA, CS and MXene are successfully integrated in the composite and potentially develop interactions [70].

3.5. XRD analysis

According to XRD analysis, PMMA exhibited (Fig. 7.B1) a semi-crystalline structure. The prominent peaks were observed at angles of 25.79°, 32.20° and 49.86°. The 32.20° peak is a frequently reported position for PMMA in the literature and confirms that it exhibits semi-crystalline properties. This crystallinity may improve the thermo-mechanical properties of PMMA. The most prominent XRD peaks of PMMA are reported between 31 and 33° [71]. These findings support that PMMA is a building block that provides rigidity as a matrix phase for e-skin applications.

According to XRD data, CS exhibited (Fig. 7.B2) a structure dominated by amorphous character. However, many weak crystalline peaks were observed such as 23.20°, 29.61°, 33.25°, 36.15°, 39.54°, and 47.65°. This indicates that chitosan is partially crystalline in nature. In particular, the peak at 29.61° is indicative of crystalline segments and is consistent with a low degree of crystallinity (~12–18 %). This value is advantageous for the water retention and biocompatibility of CS but limits its mechanical strength. According to the literature, similar patterns overlap strikingly, with large, low-density batteries between 20 and 30° reported [72].

The XRD pattern of MXene was observed (Fig. 7.B3) at an angle of 2θ = 8.4°; this peak corresponds to the (002) plane and is indicative of the interlamellar distance of MXene (d = 1.05 nm). This peak is associated with the (002) plane [73], which usually reflects the interlayer distance of MXene such as $Ti_3C_2T_x$. The values of 18.3°, 27.3°, and 33.6° correspond to the (004), (008) and (110) planes, respectively, and are indicative of disorder in the crystal phases of MXene [74–76]. This crystalline structure of MXene offers the advantage of conductivity in electronic applications such as e-skin [77,78].

The PMMA:CS composite shows (Fig. 7.B) the formation of a new peak around 16.65°. This value corresponds to neither PMMA nor CS in its pure form, indicating the presence of a new crystalline order. This peak could be an indication of new ordered structures formed as a result of physical or weak chemical interaction between PMMA and CS. The 32.20° and 49.86° batteries of PMMA are partially preserved, but their intensities are reduced. This indicates a decrease in the degree of crystallinity [79].

The PMMX composite (Fig. 7.B) retained the PMMA batteries at 32.20° and 49.53°, but the 8.4° peak of MXene was erased or lost prominence. This indicates that MXene is completely dispersed in the PMMA matrix and its layered structure is disrupted. This structure indicates that homogeneously dispersed MXene contributes to the conductivity while the crystalline structure is sacrificed [45].

In the XRD pattern for the PMMX:CS composite (Fig. 7.B), the most prominent new peak appeared at an angle of 13.91° [69]. This peak is not seen in any other sample and is probably indicative of a new phase formed between MXene and CS. The formation of this new structure may be due to electrostatic and hydrogen bonding effects. The 32.20° and 49.53° batteries of PMMA were also observed but with lower density, indicating that the crystallinity of the composite has decreased but a multiphase structure has formed. Such structures combine flexibility, conductivity and biocompatibility, providing an ideal material

infrastructure for e-skin technologies.

3.6. AFM analysis

The AFM image shown in Fig. 8 captures the material's physical structure and crystallinity. Fig. 8 shows the surface morphology of perovskite-containing PMMA passivation layers. Images A and B show the difference between PMMX:CS and PMMX compositions, respectively. In both cases, the formation of nanostructures is observed; however, the higher MX content (B) reveals a denser and more complex surface structure.

The surface roughness values in Fig. 8A and B are around ~150 nm, whereas Fig. 8.C shows a more irregular and complex formation with a surface roughness of 162 nm. The increased MX content leads to a rougher surface and notable fluctuations in the topography. Generally, smoother surfaces (lower roughness) provide better electronic properties in devices, suggesting that the higher MX content in B might need optimization, particularly for electronic applications. However, for optical devices, maintaining surface roughness at certain levels can improve performance by increasing light scattering. The increased surface irregularity with higher MX content may cause issues for e-skin materials. Smooth surfaces are preferred for better compatibility with the eye, meaning that the PMMX:CS sample with its higher roughness may lead to unfavorable results in such applications. Therefore, samples with lower MX content, like PMMX:CS, appear more ideal for e-skin production. Additionally, the rough surface observed in Fig. 8.C may negatively affect optical transparency, as light scattering and surface irregularities can degrade the optical performance of lenses. The structure in Fig. 8.D represents the surface of the e-skin material. The transparency and structure of the surface are critical in assessing the optical properties of the lens. e-skin need to exhibit smooth and homogeneous surfaces to maintain user comfort and optimal optical performance. Otherwise, the comfort level for the user may decrease, and the optical quality may suffer. In conclusion, compositions with lower MX content, such as PMMX:CS seem more suitable for e-skin applications. Lower surface roughness offers advantages in terms of both user comfort and optical performance. On the other hand, high MX content might be more appropriate for optical or electronic devices but should be carefully considered for biomedical applications like e-skin.

3.7. N_2 adsorption-desorption analysis

BET Surface Area (S_{BET}), directly affects the adsorption capacity of the material. A higher surface area indicates that the material can perform more surface reactions. In Table 3, it was observed that after double-side etching for 15 min, the surface area (4.577 m^2/g) was the highest, indicating that more of the material's surface was exposed and the pore structure was more orderly. This is beneficial in applications like biosensors and materials requiring a large contact surface. Pore size determines the size of molecules that can pass through the material. After double-side etching, the smallest pore size (8.1 nm adsorption, 8.8 nm desorption) is observed. Smaller pore sizes allow for more controlled filtration. In applications such as e-skin, smaller pores enhance breathability while improving conformity to the eye. Pore volume indicates how much space is available inside the material for the absorption of gases or liquids. Compared to non-etched material, after double-side etching, there is a slight decrease in pore volume (0.009–0.008 cm^3/g), which may suggest that the material's pore structure becomes more compact, potentially improving stability. Lower pore volume is advantageous for e-skin materials because it helps maintain an optimal level of

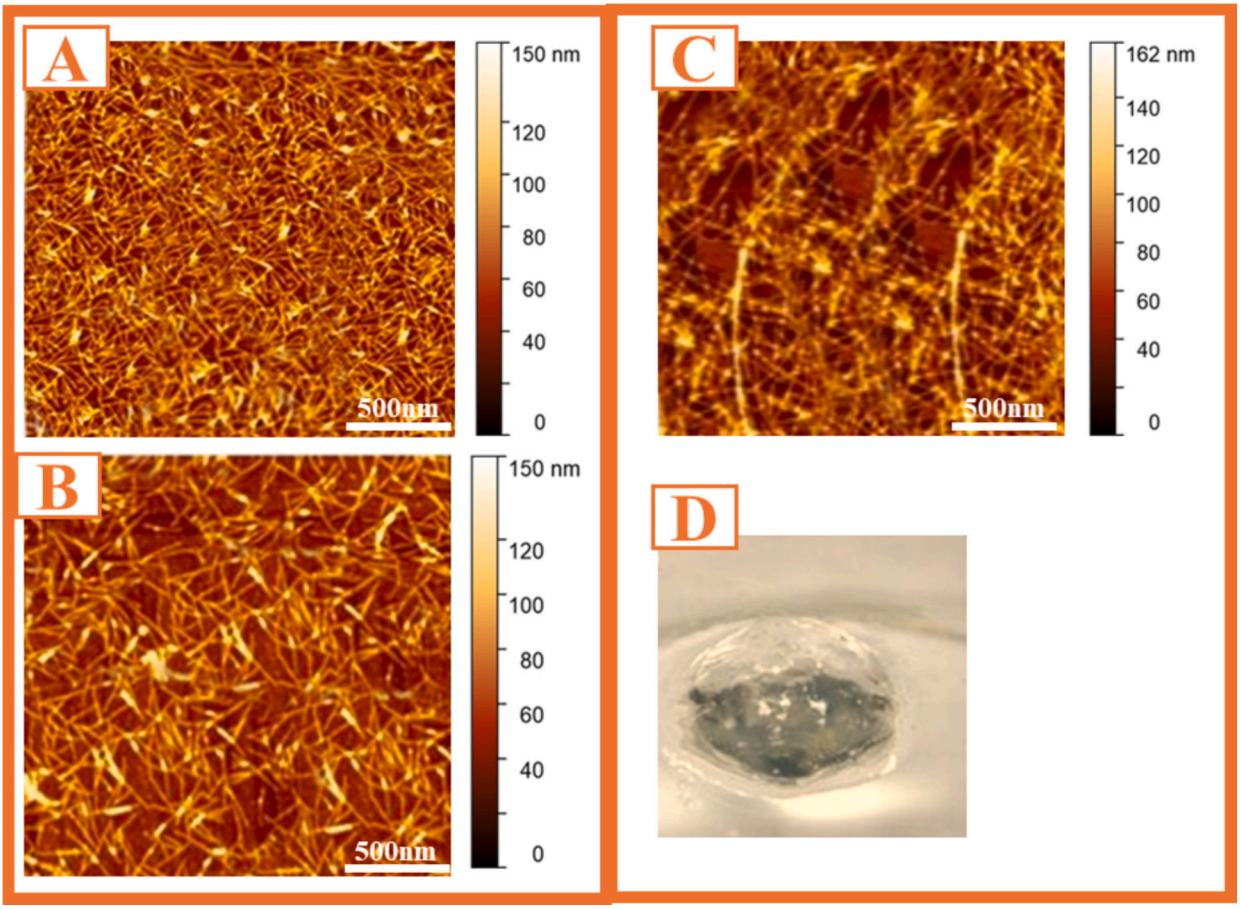

Fig. 8. AFM images of perovskite containing A. PMMA B. PMMX and C. PMMX:CS passivation layers, D. Image of PMMX:CS composite e-skin scaffold.

Table 3
BET surface area, pore size, and pore volume of PMMX:CS sensing materials obtained through various processes.

Treatment condition fiber	S_{BET} ($m^2 \bullet g^{-1}$)	Pore Size (nm)		Pore Volume ($cm^3 \bullet g^{-1}$)	
		BJH adsorption	BJH desorption	BJH adsorption	BJH desorption
Nonetched fiber	4.482	10.4	11.4	0.012	0.012
30 Min Single-Side-Etched fiber	2.329	14.5	14.0	0.006	0.006
15 Min Double-Side-Etched fiber	4.577	8.1	8.8	0.009	0.008

moisture within the lens.

The data in Table 2. suggest that the double-side etching process, by reducing pore sizes and increasing BET surface area, may have created a more effective material. In biomedical applications like e-skin, smaller pores could be better for eye health, enhancing breathability and providing better conformation to the eye surface. Additionally, the high surface area may allow for better binding of biomolecules or moisturizing agents on the lens surface. The mechanical results and pore characteristics obtained in this study, particularly regarding BET surface area and pore size, show promising performance when compared to various studies in the literature. Wei et al. [80] reported that MXene-incorporated membranes exhibited high BET surface areas, leading to efficient solvent permeation and molecular separation. In their study, membranes with a BET surface area around 4.5 m^2/g were able to perform these tasks successfully. Similarly, in our work, the BET surface area reached 4.577 m^2/g after the double-side etching process. This demonstrates that our materials also possess a high surface reaction capacity, making them suitable for biomedical applications. Another study by Huang and Liu [81] highlighted the importance of controllable pore sizes in graphene oxide membranes. In their work, smaller pore sizes (around 8–9 nm) were shown to be critical for regulating molecular transport. The pore sizes obtained in our study (8.1–8.8 nm) are similarly small, making them highly suitable for controlled filtration applications. In biomedical products such as e-skin, these smaller pores enhance breathability and biocompatibility. This indicates that our materials can be an excellent alternative for biomedical use. Furthermore, Liu et al. [82] demonstrated that reducing pore volume improved membrane stability in RGO/MOF-modified nanocomposites. In our study, the reduction in pore volume, particularly after double-side etching, shows that our materials have become more compact and stable. This is crucial for maintaining material stability in long-term biomedical applications. In this context, the results obtained in our study are consistent with other studies in the literature, demonstrating that our material offers high performance in both mechanical and surface properties. Parameters such as BET surface area, pore size, and volume point to a material structure that is highly suitable for e-skin applications.

3.8. Antimicrobial analysis

Table 4 presents the antimicrobial effects of PMMA, CS, MXene, and their combinations (PMMA:CS, PMMX, and PMMX:CS) e-skin scaffolds against multidrug-resistant bacteria and yeast. Two methods were used: disk diffusion (100 mg/mL) and well diffusion (50 mg/mL). The diameter of the inhibition zones formed around the microorganisms was measured in millimeters and reported with ± standard deviation (SD) to compare the effectiveness of the different samples.

Table 4
Assessment of antimicrobial effectiveness for tested e-skin scaffolds that coded as PMMA:CS; PMMX:CS; and PMMX and pure PMMA, CS, MXene using polymerized and un-polymerized forms via agar well and disk diffusion methods respectively by recording inhibition zones (mm ± SD).

Multidrug-resistant strains	Disk diffusion method (100 mg/mL)						Well diffusion method (50 mg/mL)					
	PMMA	CS	MXene	PMMA:CS	PMMX:CS	PMMX	PMMA	CS	MXene	PMMA:CS	PMMX:CS	PMMX
Escherichia coli	4.1 ± 0.1*	3.0 ± 0.2*	0	6.2 ± 0.2*	9.4 ± 0.3*	5.8 ± 0.3*	3.2 ± 0.2*	2.8 ± 0.3*	0	18.2 ± 1.0*	26.8 ± 1.3*	15.1 ± 0.9*
Enterobacter aerogenes	7.3 ± 0.3*	5.9 ± 0.3*	0	7.5 ± 0.3*	10.1 ± 0.2*	6.1 ± 0.4*	6.1 ± 0.2*	5.5 ± 0.2*	0	14.5 ± 0.7*	29.2 ± 1.2*	16.0 ± 0.6*
Klebsiella pneumoniae	8.5 ± 0.2*	7.1 ± 0.3*	0	7.8 ± 0.2*	11.2 ± 0.5*	6.4 ± 0.3*	7.4 ± 0.4*	6.3 ± 0.2*	0	13.1 ± 0.5*	28.7 ± 0.8*	15.6 ± 0.7*
Enterobacter cloacae	0	0	0	5.1 ± 0.4*	8.9 ± 0.3*	5.3 ± 0.2*	0	0	0	11.4 ± 0.4*	25.6 ± 0.9*	14.8 ± 0.8*
Pseudomonas aeruginosa	3.1 ± 0.1*	2.4 ± 0.2*	0	6.3 ± 0.3*	10.6 ± 0.2*	6.0 ± 0.2*	2.5 ± 0.3*	2.0 ± 0.2*	0	12.3 ± 0.5*	27.2 ± 1.1*	15.0 ± 0.4*
Staphylococcus aureus	2.2 ± 0.2*	1.7 ± 0.1*	0	5.9 ± 0.1*	9.8 ± 0.3*	5.5 ± 0.2*	1.9 ± 0.1*	1.5 ± 0.2*	0	10.9 ± 0.2*	26.1 ± 0.7*	14.7 ± 0.5*
Salmonella typhimurium	3.2 ± 0.1*	2.1 ± 0.1*	0	5.6 ± 0.2*	9.3 ± 0.2*	5.2 ± 0.2*	2.4 ± 0.2*	2.0 ± 0.1*	0	11.7 ± 0.6*	25.7 ± 0.6*	13.8 ± 0.4*
Bacillus cereus	5.1 ± 0.3*	4.2 ± 0.3*	0	6.8 ± 0.2*	10.9 ± 0.4*	6.0 ± 0.2*	4.5 ± 0.2*	3.9 ± 0.2*	0	13.5 ± 0.6*	28.3 ± 0.5*	15.9 ± 0.3*
Listeria monocytogenes	0	0	0	5.2 ± 0.3*	9.6 ± 0.4*	5.3 ± 0.1*	0	0	0	12.2 ± 0.3*	26.4 ± 0.6*	14.6 ± 0.4*
Streptococcus pneumoniae	0	0	0	5.0 ± 0.2*	9.7 ± 0.3*	5.4 ± 0.2*	0	0	0	10.4 ± 0.5*	27.8 ± 0.4*	15.2 ± 0.2*
Bacillus pumilus	3.3 ± 0.2*	2.6 ± 0.2*	0	6.1 ± 0.3*	9.9 ± 0.2*	5.7 ± 0.3*	2.8 ± 0.1*	2.2 ± 0.1*	0	12.1 ± 0.3*	26.5 ± 0.6*	14.5 ± 0.3*
Candida albicans	12.6 ± 0.3*	10.7 ± 0.4*	0	17.2 ± 0.2*	12.75 ± 0.02*	6.2 ± 0.2*	11.5 ± 0.3*	9.8 ± 0.2*	0	16.4 ± 0.6*	30.9 ± 0.7*	17.6 ± 0.5*

* Statistical analysis was performed using one-way ANOVA followed by Tukey's post-hoc test ($p < 0.05$).

Firstly, it is observed that the three main materials tested, PMMA, CS, and MXene, generally form very low inhibition zones when used alone. In particular, the fact that MXene showed no inhibition against any microorganism species (0 mm) clearly demonstrates that this substance alone has no antimicrobial activity. This shows that MXene can only reveal its antimicrobial potential when used in a suitable carrier matrix. However, it was observed that PMMA and CS could produce limited inhibition against some microorganisms. Especially against yeast species such as *Candida albicans*, a moderate antimicrobial effect was obtained with PMMA (disk diffusion: 12.6 mm; well diffusion: 11.5 mm) and CS (disk diffusion: 10.7 mm; well diffusion: 9.8 mm). However, when evaluated in terms of bacterial species, the antimicrobial activity of these two components alone was very limited and inhibition zones were mostly measured in the range of 2–5 mm [43,48].

The composited PMMX:CS formulation demonstrated remarkable antimicrobial efficacy, standing out as the most effective combination in both disk diffusion and well diffusion assays. It produced the largest inhibition zones against all tested microorganisms. According to the disk diffusion results, the PMMX:CS composite exhibited nearly double the inhibitory effect compared to individual components against strains such as *Enterobacter aerogenes* (10.1 mm), *Klebsiella pneumoniae* (11.2 mm), *Bacillus cereus* (10.9 mm), and *Candida albicans* (12.75 mm). This trend was even more pronounced in the well diffusion data, where significantly larger inhibition zones were recorded 30.9 mm for *Candida albicans*, 29.2 mm for *Enterobacter aerogenes*, and 28.7 mm for *Klebsiella pneumoniae* clearly demonstrating the high antimicrobial potential of the composited PMMX:CS formulation [83,84].

Although the PMMA:CS and PMMX formulations exhibited significantly enhanced antimicrobial activity compared to their individual components, their performance remained relatively weaker when compared to the PMMX:CS formulation. The PMMA:CS composite generally showed moderate inhibitory effects, with an inhibition zone of 18.2 mm observed against *E. coli*, for example. In contrast, the PMMX formulation produced a smaller inhibition zone of 15.1 mm against the same strain. This disparity highlights the potential synergistic interaction between chitosan and MXene when combined. It also suggests that the polymeric matrix not only enhances the inherent antimicrobial activity of MXene but may also facilitate the diffusion of active agents toward the target microorganisms, thereby contributing to the superior efficacy observed in the PMMX:CS composite [44,51,85].

Among the Gram-negative bacteria, the PMMX:CS formulation produced the highest inhibition zones in a statistically significant manner, particularly against strains such as *Escherichia coli, Enterobacter aerogenes, and Klebsiella pneumoniae*. The fact that these bacteria typically possess outer membrane structures associated with high resistance further underscores the significance of the observed antimicrobial effects. A similar trend was also observed in Gram-positive bacteria (*Staphylococcus aureus, Bacillus cereus, Streptococcus pneumoniae*), where inhibition zones exceeding 25 mm were particularly evident in the well diffusion assay, highlighting the broad-spectrum efficacy of the PMMX:CS formulation [86,87].

Another important finding is the complete lack of antimicrobial activity exhibited by the individual base components against certain microorganisms. For example, *Listeria monocytogenes* and *Streptococcus pneumoniae* showed no measurable inhibition zones when treated with PMMA, CS, or MXene individually. In contrast, the PMMX:CS formulation produced notable inhibition zones of 26.4 mm and 27.8 mm, respectively, against these strains. These results underscore the broad-spectrum and potent antimicrobial efficacy of the composite formulation. Asterisks (*) in the data tables denote combinations that yielded statistically significant differences. Tukey's post-hoc analysis further confirmed these differences, revealing that PMMX:CS performed significantly better than all other formulations. Thus, the observed outcomes are supported not only by biological evidence but also by robust statistical validation.

Table 4 provides a comprehensive overview of the antimicrobial efficacy of the various formulations against multidrug-resistant pathogens. Among these, the PMMX:CS formulation demonstrated the most pronounced effect, both in numerical terms and with statistical significance. The observed synergy between chitosan and MXene suggests that this formulation holds strong potential for clinical applications. Its broad-spectrum activity—particularly against commonly resistant bacterial and fungal strains such as *Candida albicans*—indicates that PMMX:CS could serve as a promising candidate for the development of next-generation antimicrobial e-skin scaffolds [88].

Table 5 evaluates the antimicrobial efficacy of the unpolymerized form of the PMMA:CS composite hydrogel scaffold against multidrug-resistant pathogenic microorganisms based on concentration. This assessment was conducted by measuring the inhibition rates (%) against each tested microorganism at concentrations of 20, 40, 60, 80, and 100 mg/mL. These rates indicate the extent to which the material suppresses microbial growth and reveal the trend of the minimum inhibitory concentration (MIC). In this respect, the table not only demonstrates the antimicrobial potential but also allows us to analyze the effective dose ranges of this potential. According to the data in the table, the PMMA:CS formulation exhibits a dose-dependent antimicrobial activity profile. In general, inhibition rates increase with rising concentrations, indicating that the formulation's efficacy is sensitive to dosage. Even at a relatively low concentration of 20 mg/mL, inhibition rates ranging from 17 % to 23 % were observed against certain microorganisms. These values are particularly significant in the context of MDR (multidrug-resistant) pathogens, as many conventional antibiotics fail to exhibit any effect at such low concentrations. From this perspective, the formulation appears capable of suppressing microbial growth even at minimal doses [60,89].

At the highest tested concentration of 100 mg/mL, the PMMA:CS formulation exhibited inhibition rates exceeding 50 % across all microorganisms, with values reaching between 60 % and 67 % for certain species. These results indicate that formulation functions as a highly effective antimicrobial agent, particularly at elevated concentrations. The highest inhibition was observed against *Candida albicans* at 67.2 %, representing the most potent response among all microorganism–material combinations. This was followed by *Bacillus cereus* (65.1 %), *Staphylococcus aureus* (63.7 %), and *Klebsiella pneumoniae* (62.4 %). Collectively, these findings suggest that the PMMA:CS formulation exhibits stronger antimicrobial activity against Gram-positive bacterial and fungal pathogens [90,91].

When examining the inhibition percentages for each pathogen, it is notable that some species show little to no effect at lower concentrations. For example, the inhibition rate at 20 mg/mL is 0 % for *Enterobacter cloacae, Listeria monocytogenes*, and *Streptococcus pneumoniae*. This may indicate that these species are more resistant to low doses or that the active components of the hydrogel are less effective against the cell wall structures of these pathogens. However, significant inhibition begins at 40 mg/mL even for these species. Notably, *E. cloacae* shows a meaningful inhibition rate of 51.6 % at 100 mg/mL. Another noteworthy microorganism is *Candida albicans*, which exhibited consistently high inhibition rates across all tested concentrations, indicating a pronounced sensitivity to the hydrogel formulation. This suggests that the antifungal activity of the PMMA:CS composite may be even more potent than its antibacterial effects. Given the rising incidence of antifungal-resistant infections, this finding is of considerable clinical significance.

When evaluated in terms of Gram-negative bacteria (such as *E. coli, K. pneumoniae, P. aeruginosa*), inhibition rates are generally lower than Gram-positive bacteria. For example, the highest inhibition rate for *P. aeruginosa* was 60.3 %. Nevertheless, this value still reflects a remarkable antimicrobial effect, particularly given the well-known resistance profile of this pathogen. The inhibitory effect of the formulation begins to increase significantly at concentrations starting from 40 mg/mL. The 40–80 mg/mL range appears to be the most effective dose interval, during which inhibition rates rise most sharply, indicating optimal antimicrobial performance of the PMMA:CS formulation. Although inhibition continues to increase beyond 80 mg/mL, the rate of

Table 5
Detection of the minimum inhibitory concentration (MIC) for un-polymerized of PMMA:CS e-skin scaffold (20, 40, 60, 80, and 100 mg/mL) against multi-drug-resistant pathogens by measuring of the inhibitory proportional factor (%).

Multidrug-resistant strains	Un-polymerized PMMA:CS (mg/mL)				
	20	40	60	80	100
Escherichia coli	18.5 ± 1.2	36.8 ± 2.1	44.2 ± 2.5	52.6 ± 3.1	61.5 ± 1.7
Enterobacter aerogenes	17.2 ± 0.9	33.4 ± 2.6	40.3 ± 1.8	48.7 ± 2.4	59.1 ± 1.3
Klebsiella pneumoniae	21.7 ± 1.5	39.6 ± 2.2	46.1 ± 3.0	54.3 ± 1.8	62.4 ± 2.7
Enterobacter cloacae	0	28.5 ± 2.4	35.7 ± 2.2	43.8 ± 1.5	51.6 ± 1.1
Pseudomonas aeruginosa	19.1 ± 1.1	38.2 ± 1.7	44.9 ± 2.0	52.5 ± 2.9	60.3 ± 1.8
Staphylococcus aureus	20.6 ± 0.8	39.7 ± 1.2	47.6 ± 2.5	55.2 ± 2.3	63.7 ± 2.0
Salmonella typhimurium	18.3 ± 1.4	36.3 ± 1.6	43.1 ± 2.4	50.8 ± 2.1	58.6 ± 2.3
Bacillus cereus	22.8 ± 1.6	41.2 ± 2.7	49.0 ± 3.1	56.4 ± 2.8	65.1 ± 2.5
Listeria monocytogenes	0	31.6 ± 1.9	39.5 ± 2.3	47.2 ± 2.6	55.8 ± 2.2
Streptococcus pneumoniae	0	30.7 ± 2.0	38.2 ± 1.7	46.0 ± 1.8	54.3 ± 2.6
Bacillus pumilus	19.4 ± 1.2	37.3 ± 2.4	45.1 ± 2.6	53.6 ± 2.0	62.0 ± 1.9
Candida albicans	23.5 ± 1.9	42.1 ± 2.2	50.8 ± 2.4	58.3 ± 2.5	67.2 ± 2.7

Inhibitory proportional factor (% ± SD).

improvement slows considerably in some species, with values leveling off around 60–65 %. This suggests that higher concentrations may provide only limited additional benefits [92].

Based on this comprehensive analysis, the PMMA:CS formulation was found to exhibit broad spectrum and potent antimicrobial activity, especially at high concentrations. While high inhibition rates were obtained against Gram-positive bacteria and yeast species, it showed moderate activity against Gram-negative bacteria. These findings suggest that the un-polymerized form of PMMA:CS can be used as a potential local antimicrobial agent. In addition, its ineffectiveness in some species at low concentrations emphasizes the importance of dose optimization for the target pathogen in the product development process.

Table 6 presents the antimicrobial activity of the MXene-based polymer matrix PMMX hydrogel scaffold (in its unpolymerized form) against multidrug-resistant microorganisms, measured as inhibition percentages at various concentrations (20, 40, 60, 80, and 100 mg/mL). This formulation aims to reveal the effect of MXene within the PMMA matrix and is critically important for understanding the antimicrobial performance of MXene in a carrier matrix, especially considering previous data showing that MXene alone is ineffective [93,94].

The first notable observation is that at 20 mg/mL, no inhibition was observed against any microorganism (0 % inhibition). This clearly indicates that the PMMX formulation does not exhibit antimicrobial activity at low concentrations. This finding provides an important structural insight: MXene must surpass a certain threshold concentration to be effective. At low concentrations, MXene particles dispersed within the polymer matrix may not be present in sufficient density to contact microorganisms, or compound release at these levels may be inadequate.

Inhibition begins at 40 mg/mL, but the rates remain relatively low across all microorganisms. Inhibition percentages at 40 mg/mL generally range between 19.8 % and 27.6 %. These values indicate that the PMMX formulation's activity only starts at a moderate level and increases gradually before reaching saturation. At 100 mg/mL, inhibition rates rise to between 35 % and 43 % for all microorganisms. This represents a lower maximum inhibition level compared to the PMMA:CS formulation analyzed in the previous table.

For instance, *Staphylococcus aureus* and *Candida albicans* appear to be among the most sensitive species to this formulation, exhibiting inhibition rates of 41.3 % and 43.5 %, respectively. However, species such as *Escherichia coli* (38.2 %), *Pseudomonas aeruginosa* (37.8 %) and *Enterobacter cloacae* (35.6 %) remain at these inhibition levels. The overall trend presented in the table indicates that the MXene-based formulation is more effective against Gram-positive organisms, while its efficacy against Gram-negative bacteria remains relatively limited. This situation can be attributed to the outer membranes of Gram-negative bacteria being more resistant to diffusion. Increases in inhibition values associated with dose increases are not linear. While a relatively rapid increase is observed in the 40–60 mg/mL range, the rate of increase slows significantly in the 80–100 mg/mL range. For example, the inhibition rate for *Listeria monocytogenes*, which is 25.1 % at 40 mg/mL, increases to only 27.0 % at 60 mg/mL and reaches 40.6 % at 100 mg/mL. This indicates that while the formulation increases its efficacy above a certain concentration, the efficiency rate decreases and approaches saturation. Similar trends are observed in species such as *Bacillus cereus, Klebsiella pneumoniae*, and *Streptococcus pneumoniae.* When compared to Table 5, the inhibition rates of the PMMX formulation are generally lower. For example, while the PMMA:CS formulation provides 62.4 % inhibition at 100 mg/mL for *Klebsiella pneumoniae*, PMMX shows only 40.1 % inhibition at the same concentration. This difference is even more pronounced for *Candida albicans*; the inhibition rate of 67.2 % in the PMMA:CS formulation remains at 43.5 % in PMMX. This comparison demonstrates that the presence of CS significantly enhances MXene's antimicrobial efficacy, suggesting that hybrid systems like PMMX:CS could offer a much stronger effect. The PMMX formulation has a limited but stable inhibitory profile that begins to show its effect when a certain concentration threshold is exceeded, rather than being a directly potent antimicrobial agent [20]. In clinical applications, this type of formulation may be preferred as a supportive antimicrobial agent, especially for

Table 6
Determination of the minimum inhibitory concentration (MIC) for un-polymerized of PMMX sample (20, 40, 60, 80, and 100 mg/mL) against multi-drug-resistant pathogens by calculating the inhibitory proportional factor (%).

Multidrug-resistant strains	Un-polymerized PMMX (mg/mL)				
	20	40	60	80	100
Escherichia coli	0.0	21.5 ± 1.2	23.6 ± 0.9	30.3 ± 1.1	38.2 ± 1.0
Enterobacter aerogenes	0.0	19.8 ± 0.8	21.4 ± 0.5	28.7 ± 1.3	36.9 ± 0.9
Klebsiella pneumoniae	0.0	24.2 ± 1.0	26.1 ± 0.7	33.5 ± 0.9	40.1 ± 0.8
Enterobacter cloacae	0.0	20.1 ± 1.2	22.3 ± 1.1	29.8 ± 0.7	35.6 ± 0.6
Pseudomonas aeruginosa	0.0	22.6 ± 0.9	24.7 ± 0.8	31.0 ± 0.8	37.8 ± 0.5
Staphylococcus aureus	0.0	25.8 ± 1.1	27.2 ± 0.9	34.4 ± 1.0	41.3 ± 1.2
Salmonella typhimurium	0.0	23.5 ± 1.0	25.1 ± 0.8	32.2 ± 1.1	39.7 ± 1.0
Bacillus cereus	0.0	26.4 ± 1.3	28.3 ± 1.2	35.6 ± 1.0	42.1 ± 0.9
Listeria monocytogenes	0.0	25.1 ± 1.2	27.0 ± 0.8	34.2 ± 0.7	40.6 ± 1.1
Streptococcus pneumoniae	0.0	26.8 ± 0.9	28.7 ± 0.7	35.9 ± 1.3	41.7 ± 0.8
Bacillus pumilus	0.0	25.9 ± 1.1	27.4 ± 0.9	34.7 ± 0.6	40.3 ± 0.7
Candida albicans	0.0	27.6 ± 1.0	29.8 ± 0.9	37.4 ± 1.2	43.5 ± 1.1

Inhibitory proportional factor (% ± SD).

local treatments targeting Gram-positive pathogens. However, for cases requiring broad-spectrum and high-level inhibition, the addition of CS appears indispensable.

The data in Table 6 show that the PMMX formulation exhibits antimicrobial activity due to its MXene content, but that this activity remains moderate. Its complete ineffectiveness at low concentrations suggests that MXene is unable to achieve sufficient contact density within the carrier polymer matrix. Moreover, inhibition rates not exceeding 50 % even at high doses indicate that the formulation alone is not an optimal antimicrobial solution. In this context, when used in combination with CS (as shown in the next table, PMMX:CS), the PMMX formulation demonstrates significantly stronger and clinically applicable antimicrobial performance [22,95].

Table 7 shows the antimicrobial activity of the PMMX:CS (i.e., MXene + PMMA + CS) formulation against multidrug-resistant microorganisms at different concentrations (20, 40, 60, 80, and 100 mg/mL) as inhibition percentages. This formulation represents the most effective antimicrobial profile data, thanks to the synergistic combination of its components, when evaluated in the context of the previous three tables. The most notable difference between the PMMX:CS formulation and the other two formulations (PMMA:CS and PMMX) is that it provides significant inhibition even at the lowest concentration. At a concentration of 20 mg/mL, inhibition rates range from 44.6 % to 55.4 % in all microorganisms. These values are significantly higher compared to the previous two formulations; for example, PMMA:CS showed 0 % inhibition in some species (e.g., *Listeria monocytogenes*) at the same concentration, while PMMX showed no inhibition in any species. This early effect clearly demonstrates the strong synergistic action of the PMMX:CS combination. The structural properties formed by the combined components (MXene, PMMA, and CS) likely facilitate early penetration into microbial cell membranes. Perhaps the most striking finding is that even at the relatively low concentration of 40 mg/mL, the formulation achieves the highest inhibition rates across many species. For example, inhibition rates reached 80.6 % for *Candida albicans*, 79.0 % for *Streptococcus pneumoniae*, 78.6 % for *Staphylococcus aureus*, 77.8 % for *Bacillus cereus*, and 76.4 % for *Listeria monocytogenes*. All these species are clinically significant, multidrug-resistant pathogens. Particularly in fungal species such as *Candida albicans*, where conventional antibiotics demonstrate limited efficacy, the observed level of inhibition highlights the remarkable antifungal potential of the material [96,97]. Furthermore, these substantial inhibition rates suggest that this formulation could serve as a promising alternative to traditional antibiotics, especially in cases where standard treatments fail to provide adequate effectiveness.

After reaching a concentration of 40 mg/mL, an interesting trend is observed in the inhibition rates: as the dose increases, the inhibition effect begins to decrease. For example, the inhibition rate for *Escherichia coli* is 71.6 % at 40 mg/mL, but drops to 52.4 % at 100 mg/mL. Similarly, a decrease from 75.2 % to 53.0 % was recorded for *Pseudomonas aeruginosa*, and from 74.3 % to 51.7 % for *Salmonella typhimurium*. These findings indicate a deviation from the classic dose-response relationship and suggest an inverted U-shaped effect curve—beyond a certain point, increasing the concentration causes a decrease rather than an increase in antimicrobial activity. This effect can be explained by several potential mechanisms. At high concentrations, the aggregation of MXene or CS particles may reduce surface activity, thereby limiting antimicrobial effectiveness. Additionally, increased material density increases the gelation, which can create a diffusion constraint by preventing the active components from spreading to surrounding tissues. Furthermore, adding a high amount of material to the environment can disrupt pH and ionic balance, thereby suppressing some antimicrobial effects. Considering all these factors, it is understood that the antimicrobial efficacy of the PMMX:CS formulation reaches its highest level within a specific concentration range (particularly between 40 and 60 mg/mL) and that bioavailability decreases above this threshold. This situation indicates that careful optimisation is required in the dosage planning of the formulation and that maximum efficacy is achieved within this concentration range.

Table 7 shows that the PMMX:CS formulation is highly effective against all groups of microorganisms. However, it has been noted that the inhibition values contain some systematic differences based on species. In particular, the average inhibition rates for Gram-positive bacteria (*S. aureus, B. cereus, L. monocytogenes, S. pneumoniae*) were above 70 % across the entire concentration range. Inhibition rates against Gram-negative bacteria (*E. coli, E. aerogenes, K. pneumoniae, P. aeruginosa, S. typhimurium*) remained within the average range of 65–70 %. Although this difference is small, it indicates that the formulation exhibits a stronger effect against Gram-positive bacteria.

The achievement of the highest inhibition rate of 80.6 % on *Candida albicans* suggests that the material can be used not only as an antibacterial agent but also as an effective antifungal agent. Since fungi have a different cell wall structure, inhibition at this level is quite remarkable. The PMMX:CS formulation is a broad-spectrum, highly effective antimicrobial agent that acts quickly even at low concentrations. This makes it a highly promising candidate for combating multidrug-resistant pathogens across both bacterial and fungal targets. Such a biomaterial holds great potential for various clinical applications, including wound healing, biosensor surface coatings, implant sterilization, and localized infection control. By combining the structural contribution of MXene with the natural antimicrobial properties of CS, the PMMX:CS formulation achieves high inhibition rates against all tested pathogens. The effective dose range is concentrated around 40–60 mg/mL, with inhibition rates decreasing above this range. These results indicate that the formulation can be adapted for practical use with careful dose

Table 7
Determination of the minimum inhibitory concentration (MIC) for un-polymerized of PMMX:CS sample (20, 40, 60, 80, and 100 mg/mL) against multi-drug-resistant pathogens by calculating the inhibitory proportional factor (%).

Multidrug-resistant strains	Un-polymerized PMMX:CS (mg/mL)				
	20	40	60	80	100
Escherichia coli	49.2 ± 1.2	71.6 ± 1.9	56.8 ± 2.3	54.2 ± 1.6	52.4 ± 1.8
Enterobacter aerogenes	45.7 ± 1.0	68.3 ± 2.1	53.2 ± 2.0	50.6 ± 1.7	48.1 ± 1.4
Klebsiella pneumoniae	47.8 ± 1.5	73.4 ± 2.5	55.4 ± 2.8	52.8 ± 2.1	50.3 ± 2.2
Enterobacter cloacae	44.6 ± 1.4	70.5 ± 2.4	52.7 ± 2.3	50.2 ± 1.8	47.6 ± 1.5
Pseudomonas aeruginosa	51.0 ± 1.3	75.2 ± 2.0	58.1 ± 2.2	55.3 ± 1.9	53.0 ± 1.8
Staphylococcus aureus	50.2 ± 1.5	78.6 ± 2.6	59.4 ± 2.5	56.1 ± 2.3	54.8 ± 2.0
Salmonella typhimurium	47.3 ± 1.6	74.3 ± 2.1	56.1 ± 2.4	53.6 ± 1.9	51.7 ± 1.6
Bacillus cereus	53.1 ± 1.9	77.8 ± 2.8	60.4 ± 2.7	57.2 ± 2.4	55.6 ± 2.1
Listeria monocytogenes	50.7 ± 1.7	76.4 ± 2.2	58.3 ± 2.3	55.1 ± 2.0	53.7 ± 1.9
Streptococcus pneumoniae	52.6 ± 1.4	79.0 ± 2.3	59.7 ± 2.4	56.6 ± 2.2	54.1 ± 1.7
Bacillus pumilus	48.2 ± 1.3	72.9 ± 2.0	56.0 ± 2.1	53.5 ± 1.8	51.2 ± 1.5
Candida albicans	55.4 ± 1.8	80.6 ± 2.7	61.9 ± 2.9	58.3 ± 2.6	57.1 ± 2.3

Inhibitory proportional factor (% ± SD).

adjustments, offering both effective and economical application. Thanks to its structural versatility and broad antimicrobial spectrum, PMMX:CS stands out as a strong candidate for future applications in e-skin systems.

4. Conclusion

This study successfully developed PMMA-based electrospun nanofiber composites incorporating MXene and CS, demonstrating significantly enhanced mechanical, electrical, and antimicrobial performance. The addition of MXene improved tensile strength, conductivity, and surface crystallinity, while chitosan further optimized flexibility, insulation, and biocompatibility. Specific surface and pore size analyses showed that the composite's microstructure is well-suited for breathability and durability, critical for e-skin applications. Importantly, antimicrobial assays confirmed that Chitosan-MXene synergy effectively inhibits multidrug-resistant pathogens, outperforming individual components. These findings highlight the potential of PMMA-MXene-CS composites as multifunctional, high-performance materials for biomedical and wearable applications, particularly e-skin. Future studies should focus on in vivo assessments and long-term stability to advance clinical translation.

Supplementary information

Not applicable.

CRediT authorship contribution statement

Berfin Gürbüz: Methodology, Investigation, Funding acquisition, Formal analysis, Data curation, Conceptualization, Writing – review & editing, Writing – original draft. **Fatih Ciftci:** Visualization, Validation, Supervision, Software, Resources, Project administration, Methodology, Investigation, Funding acquisition, Formal analysis, Data curation, Conceptualization, Writing – review & editing, Writing – original draft. **Ali Can Özarslan:** Visualization, Validation, Methodology, Investigation, Formal analysis, Data curation, Conceptualization, Writing – review & editing, Writing – original draft. **Bahar Akyuz Yilmaz:** Visualization, Validation, Methodology, Investigation, Formal analysis, Data curation, Conceptualization, Writing – review & editing, Writing – original draft.

Ethical approval

Not applicable.

Declaration of competing interest

The author declare no competing financial interests or personal relationships in this paper.

Acknowledgements

The author would like to thank Fatih Sultan Mehmet Vakıf University Technology Transfer Office and Biomedical Department BiorginAI Research Group Biomaterials nanotechnology Laboratory for supporting this study. We would like to thank Kais FARFOUR, Veterinarian at Fırat University, Faculty of Veterinary Medicine for his contributions to this article.

Data availability

The study is completely new and all data and photos are shared in this study.

References

[1] B. Sarac, S. Yücer, H. Sahin, M. Unal, F. Ciftci, Wearable and implantable bioelectronic: biosensing contact lens and applications, Chem. Eng. J. 491 (2024) 152016, https://doi.org/10.1016/j.cej.2024.152016.
[2] S.N. Lihan, B.A. Yilmaz, F. Ciftci, Functional bacterial cellulose-based MXene ($Ti_3C_2T_x$) electronic-skin patch for accelerated healing and monitoring, BME Frontiers 6 (2025) 109, https://doi.org/10.34133/bmef.0109.
[3] K. Ishihara, X. Shi, K. Fukazawa, T. Yamaoka, G. Yao, J.Y. Wu, Biomimetic-engineered silicone hydrogel contact lens materials, ACS Appl. Bio Mater. 6 (2023) 3600–3616, https://doi.org/10.1021/acsabm.3c00296.
[4] A.E. Salih, M. Elsherif, F. Alam, B. Alqattan, A.K. Yetisen, H. Butt, Syntheses of gold and silver nanocomposite contact lenses via chemical volumetric modulation of hydrogels, ACS Biomater. Sci. Eng. 8 (2022) 2111–2120, https://doi.org/10.1021/acsbiomaterials.2c00174.
[5] S. Liu, L. Jones, F.X. Gu, Nanomaterials for ocular drug delivery, Macromol. Biosci. 12 (2012) 608–620, https://doi.org/10.1002/mabi.201100419.
[6] L.R. Feksa, E.A. Troian, C.D. Muller, F. Viegas, A.B. Machado, V.C. Rech, Hydrogels for biomedical applications, in: Nanostructures for the Engineering of Cells, From Design to Applications, Tissues and Organs, 2018, pp. 403–438, https://doi.org/10.1016/B978-0-12-813665-2.00011-9.
[7] B. Gürbüz, F. Ciftci, Bio-electric-electronics and tissue engineering applications of MXenes wearable materials: a review, Chem. Eng. J. 489 (2024) 151230, https://doi.org/10.1016/J.CEJ.2024.151230.
[8] E.G. Stocker, J.P. Schoessler, Corneal endothelial polymegathism induced by PMMA contact lens wear, Investig. Ophthalmol. Vis. Sci. 26 (1985) 857–863.
[9] T.T. McMahon, Contact lenses, in: Albert and Jakobiec's Principles and Practice of Ophthalmology, Fourth edition, 2022, pp. 1023–1035, https://doi.org/10.1007/978-3-030-42634-7_238.
[10] J.H.J. Thean, A.A. Mcnab, Blepharoptosis in RGP and PMMA hard contact lens wearers, Clin. Exp. Optom. 87 (2004) 11–14, https://doi.org/10.1111/j.1444-0938.2004.tb03139.x.
[11] K. Diedkova, A.D. Pogrebnjak, S. Kyrylenko, K. Smyrnova, V.V. Buranich, P. Horodek, P. Zukowski, T.N. Koltunowicz, P. Galaszkiewicz, K. Makashina, V. Bondariev, M. Sahul, M. Caplovicova, Y. Husak, W. Simka, V. Korniienko, A. Stolarczyk, A. Blacha-Grzechnik, V. Balitskyi, V. Zahorodna, I. Baginskiy, U. Riekstina, O. Gogotsi, Y. Gogotsi, M. Pogorielov, Polycaprolactone-Mxene nanofibrous scaffolds for tissue engineering, ACS Appl. Mater. Interfaces 15 (2023) 14033–14047, https://doi.org/10.1021/acsami.2c22780.
[12] A. Singh, S. Gupta, K. Kumari, P.P. Kundu, MXene-polymer nanocomposites for biomedical applications, in: MXene Nanocomposites: Design, Fabrication, and Shielding Applications, 2023, pp. 197–226, https://doi.org/10.1201/9781003281511-10.
[13] K. Ławkowska, M. Pokrywczyńska, K. Koper, L.A. Kluth, T. Drewa, J. Adamowicz, Application of graphene in tissue engineering of the nervous system, Int. J. Mol. Sci. 23 (2022), https://doi.org/10.3390/ijms23010033.
[14] S.R. Shin, R. Farzad, A. Tamayol, V. Manoharan, P. Mostafalu, Y.S. Zhang, M. Akbari, S.M. Jung, D. Kim, M. Comotto, N. Annabi, F.E. Al-Hazmi, M. R. Dokmeci, A. Khademhosseini, A bioactive carbon nanotube-based ink for printing 2D and 3D flexible electronics, Adv. Mater. 28 (2016) 3280–3289, https://doi.org/10.1002/adma.201506420.
[15] Z. Sattar, A. Hashim, Quaternary PMMA-PEG/SnO_2-SiC nanocomposite films for flexible nanodielectric and energy storage applications, Silicon 17 (2025) 1681–1692, https://doi.org/10.1007/s12633-025-03300-z.
[16] Z. Sattar, A. Hashim, Synthesis of PMMA/PEG/SiO2/SiC multifunctional nanostructures and exploring the microstructure and dielectric features for flexible nanodielectric applications, Silicon 16 (2024) 6181–6192, https://doi.org/10.1007/s12633-024-03138-x.
[17] Z. Sattar, A. Hashim, Fabrication and characteristics of PMMA–PEG/SiO2–SiC quaternary nanocomposites for gamma ray shielding and flexible optoelectronics applications, J. Mater. Sci. Mater. Electron. 35 (2024) 1660, https://doi.org/10.1007/s10854-024-13435-1.
[18] H. Hosseinian, S. Hosseini, S.O. Martinez-Chapa, M. Sher, A Meta-analysis of wearable contact lenses for medical applications: role of electrospun Fiber for drug delivery, Polymers 14 (2022), https://doi.org/10.3390/polym14010185.
[19] P. Mehta, A.A. Al-Kinani, M.S. Arshad, M.W. Chang, R.G. Alany, Z. Ahmad, Development and characterisation of electrospun timolol maleate-loaded polymeric contact lens coatings containing various permeation enhancers, Int. J. Pharm. 532 (2017) 408–420, https://doi.org/10.1016/j.ijpharm.2017.09.029.
[20] A. Hashim, I.R. Agool, K.J. Kadhim, Modern developments in polymer nanocomposites for antibacterial and antimicrobial applications: a review, J. Bionanosci. 12 (2018) 608–613, https://doi.org/10.1166/jbns.2018.1580.
[21] Y.F. Mustafa, Modern developments in the application and function of metal/metal oxide nanocomposite–based antibacterial agents, BioNanoScience 13 (2023) 840–852, https://doi.org/10.1007/s12668-023-01100-6.
[22] H. Ahmed, A. Hashim, H.M. Abduljalil, Analysis of structural, electrical and electronic properties of (polymer nanocomposites/ silicon carbide) for antibacterial application, Egypt. J. Chem. 62 (2019) 1167–1176, https://doi.org/10.21608/EJCHEM.2019.6241.1522.
[23] C. Yang, M. Wang, W. Wang, H. Liu, H. Deng, Y. Du, X. Shi, Electrodeposition induced covalent cross-linking of chitosan for electrofabrication of hydrogel contact lenses, Carbohydr. Polym. 292 (2022), https://doi.org/10.1016/j.carbpol.2022.119678.
[24] R.L. Jadhav, S.G. Sonwalkar, M.V. Patil, S.N. Shaikh, S.N. Belhekar, Formulation and characterization of poly sulfoxyamine grafted chitosan coated contact lens, J. Pharm. Res. Int. (2020) 49–57, https://doi.org/10.9734/jpri/2020/v32i230403.

[25] P. Chen, X. Wang, J. Kong, X. Hu, A facile route to fabricate CS/GO composite film for the application of therapeutic contact lenses, Adv. Mater. Sci. Eng. 2020 (2020), https://doi.org/10.1155/2020/8476025.
[26] J.M. Deitzel, J.D. Kleinmeyer, J.K. Hirvonen, N.C. Beck Tan, Controlled deposition of electrospun poly(ethylene oxide) fibers, Polymer (2001), https://doi.org/10.1016/S0032-3861(01)00336-6.
[27] G. Eda, J. Liu, S. Shivkumar, Solvent effects on jet evolution during electrospinning of semi-dilute polystyrene solutions, Eur. Polym. J. 43 (2007) 1154–1167, https://doi.org/10.1016/j.eurpolymj.2007.01.003.
[28] C. Chen, G. Lv, C. Pan, M. Song, C. Wu, D. Guo, X. Wang, B. Chen, Z. Gu, Poly(lactic acid) (PLA) based nanocomposites - a novel way of drug-releasing, Biomed. Mater. (2007), https://doi.org/10.1088/1748-6041/2/4/L01.
[29] I. Pešić, M. Petrović, M. Vuksanović, M. Popović, M.S. Rabasović, D. Šević, V. Radojević, Structural, optical, and mechanical characterization of PMMA-MXene composites functionalized with MEMO silane, Nanocomposites 8 (2022) 215–226, https://doi.org/10.1080/20550324.2023.2168844.
[30] X. Huang, Y. Tuersun, M. Huang, W. Lin, W. Qiu, S. Chu, Highly enhanced thermal conductivity from boron nitride nanosheets and MXene phonon resonance in 3D PMMA spheres composites, Mater. Today Sustain. 21 (2023), https://doi.org/10.1016/j.mtsust.2022.100269.
[31] I. Pešić, M. Petrović, V. Radojević, Influence of synthesis parameters on mechanical properties of nanocomposite PMMA-MXene, Tehnika 76 (2021) 545–549, https://doi.org/10.5937/tehnika2105545p.
[32] W. Jiang, S. Lee, K. Zhao, K. Lee, H. Han, J.W. Oh, H. Lee, H. Kim, C.M. Koo, C. Park, Flexible and transparent electrode of hybrid Ti3C2TXMXene-silver nanowires for high-performance quantum dot light-emitting diodes, ACS Nano 16 (2022) 9203–9213, https://doi.org/10.1021/acsnano.2c01514.
[33] K. Tan, L. Samylingam, N. Aslfattahi, M.R. Johan, R. Saidur, Investigation of improved optical and conductivity properties of poly(methyl methacrylate)-MXenes (PMMA-MXenes) nanocomposite thin films for optoelectronic applications, Open Chem. 20 (2022) 1416–1431, https://doi.org/10.1515/chem-2022-0221.
[34] K. Kadhim, I. Agool, A. Hashim, Effect of zirconium oxide nanoparticles on dielectric properties of (PVA-PEG-PVP) blend for medical application, J. Adv. Phys. 6 (2017) 187–190, https://doi.org/10.1166/jap.2017.1313.
[35] J. Li, F. Xia, Y. Liu, J. Wang, X. Su, Z. Li, H. Peng, Synthesis of MXene-based functional coatings on rigid polyurethane foam surfaces: a comparative study of layer-by-layer self-assembly and hydrothermal methods, Polym. Degrad. Stab. 220 (2024), https://doi.org/10.1016/j.polymdegradstab. 2024.110665.
[36] H. Zhou, F. Wang, Y. Wang, C. Li, C. Shi, Y. Liu, Z. Ling, Study on contact angles and surface energy of MXene films, RSC Adv. 11 (2021) 5512–5520, https://doi.org/10.1039/d0ra09125a.
[37] A. Hashim, H.M. Abduljalil, H. Ahmed, Fabrication and characterization of (PVA-TiO2)1-x/ SiCx nanocomposites for biomedical applications, Egypt. J. Chem. 63 (2020) 71–83, https://doi.org/10.21608/ejchem.2019.10712.1695.
[38] M.C. Vu, D. Mani, J.B. Kim, T.H. Jeong, S. Park, G. Murali, I. In, J.C. Won, D. Losic, C.S. Lim, S.R. Kim, Hybrid shell of MXene and reduced graphene oxide assembled on PMMA bead core towards tunable thermoconductive and EMI shielding nanocomposites, Compos. A: Appl. Sci. Manuf. 149 (2021), https://doi.org/10.1016/j.compositesa.2021.106574.
[39] M.-R. Kim, Y.T. Kim, D. Seo, S.-H. Cho, Y. Lee, C.W. Ahn, H. Han, Fabrication of Porous Carbon-Composite Nanofibers Via Electrospinning and Their Application in Ion Storage System, ECS Meeting Abstracts. MA2022-02, 2022, p. 2509, https://doi.org/10.1149/ma2022-0292509mtgabs.
[40] K. Wei, X. Su, J. Zheng, S. Liu, B. Chen, Y. Guo, Dual BaTiO3 layer-cavity assisted enhancement of copper-based surface plasmon resonance biosensor, Optik 299 (2024), https://doi.org/10.1016/j.ijleo.2024.171612.
[41] K.R. Baz Khan, A. Al-Othman, H. Al-Nashash, M. Al-Sayah, Mxene/polydimethylsiloxane (PDMS) based implantable and flexible bioelectrodes for neural sensing, in: 2023 Advances in Science and Engineering Technology International Conferences, ASET, 2023, p. 2023, https://doi.org/10.1109/ASET56582.2023.10180745.
[42] P. Iravani, S. Iravani, R.S. Varma, MXene-chitosan composites and their biomedical potentials, Micromachines 13 (2022), https://doi.org/10.3390/mi13091383.
[43] E.A. Mayerberger, R.M. Street, R.M. McDaniel, M.W. Barsoum, C.L. Schauer, Antibacterial properties of electrospun Ti3C2Tz (MXene)/chitosan nanofibers, RSC Adv. 8 (2018) 35386–35394, https://doi.org/10.1039/c8ra06274a.
[44] H. Li, J. Dai, X. Yi, F. Cheng, Generation of cost-effective MXene@polydopamine-decorated chitosan nanofibrous wound dressing for promoting wound healing, Biomater. Adv. 140 (2022), https://doi.org/10.1016/j.bioadv.2022.213055.
[45] Y. Ul Haq, I. Murtaza, S. Mazhar, N. Ahmad, A.A. Qarni, Z. Ul Haq, S.A. Khan, M. Iqbal, Investigation of improved dielectric and thermal properties of ternary nanocomposite PMMA/MXene/ZnO fabricated by in-situ bulk polymerization, J. Appl. Polym. Sci. 137 (2020), https://doi.org/10.1002/app.49197.
[46] S. Tu, L. Qiu, C. Liu, F. Zeng, Y.Y. Yuan, M.N. Hedhili, V. Musteata, Y. Ma, K. Liang, N. Jiang, H.N. Alshareef, X. Zhang, Suppressing dielectric loss in MXene/polymer nanocomposites through interfacial interactions, ACS Nano 18 (2024) 10196–10205, https://doi.org/10.1021/acsnano.4c00475.
[47] J. Zhang, J. Xu, Y. Gao, F. Qin, X. Zhu, C. Kan, Flexible silver nanowire and Ti3C2Tx MXene composite films for electromagnetic interference shielding, ACS Appl. Nano Mater. 7 (2024) 4960–4968, https://doi.org/10.1021/acsanm.3c05591.
[48] A.K. Rana, V.K. Gupta, P. Hart, F. Scarpa, V.K. Thakur, Sustainable MXene-chitosan/chitin composites for interdisciplinary applications in water purification, bio-medical, bio-sensing and electronic fields, Mater. Today Sustain. 25 (2024), https://doi.org/10.1016/j.mtsust.2024.100671.
[49] H. Li, R. Fan, F. Zhang, Z. Cui, J. Li, Y. Cai, L. Kang, X. Zhan, J. Li, D. Tian, A spider-silk-inspired soybean protein adhesive with high-strength and mildew-resistant via synergistic effect of MXene nanosheets and chitosan, Ind. Crop. Prod. 193 (2023), https://doi.org/10.1016/j.indcrop.2023.116252.
[50] Z. Tan, H. Zhao, F. Sun, L. Ran, L. Yi, L. Zhao, J. Wu, Fabrication of chitosan/MXene multilayered film based on layer-by-layer assembly: toward enhanced electromagnetic interference shielding and thermal management capacity, Compos. A: Appl. Sci. Manuf. 155 (2022), https://doi.org/10.1016/j.compositesa.2022.106809.
[51] Y. Liu, D. Xu, Y. Ding, X. Lv, T. Huang, B. Yuan, L. Jiang, X. Sun, Y. Yao, J. Tang, A conductive polyacrylamide hydrogel enabled by dispersion-enhanced MXene@chitosan assembly for highly stretchable and sensitive wearable skin, J. Mater. Chem. B 9 (2021) 8862–8870, https://doi.org/10.1039/d1tb01798e.
[52] Y. Zheng, R. Yin, Y. Zhao, H. Liu, D. Zhang, X. Shi, B. Zhang, C. Liu, C. Shen, Conductive MXene/cotton fabric based pressure sensor with both high sensitivity and wide sensing range for human motion detection and E-skin, Chem. Eng. J. 420 (2021), https://doi.org/10.1016/j.cej.2020.127720.
[53] J. Ma, K. Yang, Y. Jiang, L. Shen, H. Ma, W. Zhang, J. Zhang, N. Zhu, Foot-scale MXene film of ultrathin electronic skin for wearable motion sensors, Cell Reports Phys. Sci. 3 (2022), https://doi.org/10.1016/j.xcrp.2022.101013.
[54] J. Zhang, L. Wan, Y. Gao, X. Fang, T. Lu, L. Pan, F. Xuan, Highly stretchable and self-healable MXene/polyvinyl alcohol hydrogel electrode for wearable capacitive electronic skin, Adv. Electr. Mater. (2019), https://doi.org/10.1002/aelm.201900285.
[55] X. Du, X. Li, Y. Zhang, X. Guo, Z. Li, Y. Cao, Y. Yang, W. Wang, J. Wang, Visible transparent, infrared stealthy polymeric films with nanocoating of ITO@MXene enable efficient passive radiative heating and solar/electric thermal conversion, Nano Res. 16 (2023) 3326–3332, https://doi.org/10.1007/s12274-022-4962-6.
[56] L. Wang, B. Shi, Hydroxide conduction enhancement of chitosan membranes by functionalized MXene, Materials 11 (2018), https://doi.org/10.3390/ma11112335.
[57] S. Wu, D. Chen, W. Han, Y. Xie, G. Zhao, S. Dong, M. Tan, H. Huang, S. Xu, G. Chen, Y. Cheng, X. Zhang, Ultralight and hydrophobic MXene/chitosan-derived hybrid carbon aerogel with hierarchical pore structure for durable electromagnetic interference shielding and thermal insulation, Chem. Eng. J. 446 (2022), https://doi.org/10.1016/j.cej.2022.137093.
[58] S.N. Li, Z.R. Yu, B.F. Guo, K.Y. Guo, Y. Li, L.X. Gong, L. Zhao, J. Bae, L.C. Tang, Environmentally stable, mechanically flexible, self-adhesive, and electrically conductive Ti3C2TX MXene hydrogels for wide-temperature strain sensing, Nano Energy 90 (2021), https://doi.org/10.1016/j.nanoen.2021.106502.
[59] S.N. Li, Z.F. Zeng, X.F. He, Z.C. Xu, Y.H. Luo, Q.Y. Ni, L. Peng, L.X. Gong, Y. Li, B. Jiang, Mechanically flexible and flame-retardant cellulose nanofibril-based films integrated with MXene and chitosan, Soft Sci. 2 (2022), https://doi.org/10.20517/ss.2022.20.
[60] X. Luo, Y. Liu, R. Qin, F. Ao, X. Wang, H. Zhang, M. Yang, X. Liu, Tissue-nanoengineered hyperbranched polymer based multifunctional hydrogels as flexible "wounped treatment-health monitoring" bioelectronic implant, Appl. Mater. Today 29 (2022), https://doi.org/10.1016/j.apmt.2022.101576.
[61] H. Sosiati, F. Al-Giffary, F.A. Adil, B.P. Kamiel, R.K. Adi, Y. Yusuf, The properties of kenaf/carbon/PMMA hybrid composites by adding chitosan nano and microparticles, in: Materials Today: Proceedings, 2022, pp. 2908–2913, https://doi.org/10.1016/j.matpr.2022.06.556.
[62] N.F.A. Ghapar, H. Baharin, K.J.A. Karim, Preparation and characterization of chitosan beads grafted with poly(methyl methacrylate) for controlled release study, in: AIP Conference Proceedings, 2018, https://doi.org/10.1063/1.5047195.
[63] J. Pešić, A. Šolajić, J. Mitrić, M. Gilić, I. Pešić, N. Paunović, N. Romčević, Structural and optical characterization of titanium–carbide and polymethyl methacrylate based nanocomposite, Opt. Quant. Electron. 54 (2022), https://doi.org/10.1007/s11082-022-03674-z.
[64] P.K. Kalambate, A. Dhanjai, Y. Sinha, Y. Li, Y. Huang Shen, An electrochemical sensor for ifosfamide, acetaminophen, domperidone, and sumatriptan based on self-assembled MXene/MWCNT/chitosan nanocomposite thin film, Microchim. Acta 187 (2020), https://doi.org/10.1007/s00604-020-04366-9.
[65] G.D.S. Padilha, V.M. Giacon, J.R. Bartoli, Effect of solvents on the morphology of PMMA films fabricated by spin-coating, Polimeros 27 (2017) 195–200, https://doi.org/10.1590/0104-1428.12516.
[66] M. Punset, A. Brizuela, E. Pérez-Pevida, M. Herrero-Climent, J.M. Manero, J. Gil, Mechanical characterization of dental prostheses manufactured with PMMA–graphene composites, Materials 15 (2022), https://doi.org/10.3390/ma15155391.
[67] F. Ciftci, A.C. Özarslan, Fabrication of polycaprolactone-chitosan/curcumin polymer composite fibers and evaluation of their in vitro release kinetic behavior and antibacterial-antifungal activity, J. Sol-Gel Sci. Technol. (2023), https://doi.org/10.1007/s10971-023-06264-x.
[68] A. Bukhari, I. Ijaz, E. Gilani, A. Nazir, H. Zain, S. Muhammad, A. Bukhari, A. Shaheen, S. Hussain, Simultaneous removal of Norfloxacin, Ciprofloxacin, and copper from aqueous solution by chitosan and MXene functionalized graphene oxide ternary composite based on anion-synergistic interaction, Chem. Eng. J. 474 (2023), https://doi.org/10.1016/j.cej.2023.145890.
[69] N.R. Azeez, S.S. Salih, M. Kadhom, H.N. Mohammed, T.K. Ghosh, Enhanced termination of zinc and cadmium ions from wastewater employing plain and chitosan-modified mxenes: synthesis, characterization, and adsorption performance, Green Chem. Eng. 5 (2024) 339–347, https://doi.org/10.1016/j.gce.2023.08.003.
[70] J. Pu, Y. Gao, Z. Geng, Y. Zhang, Q. Cao, J. Yang, X. Zhao, Y. Wang, J. Wang, C. Guan, Grafted MXene assisted bifunctional hydrogel for stable and highly

sensitive self-powered fibrous system, Adv. Funct. Mater. 34 (2024), https://doi.org/10.1002/adfm.202304453.
[71] E. Shobhana, X-ray diffraction and UV-visible studies of PMMA thin films, Int. J. Modern Eng. Res. (IJMER) 2 (2012) 1092–1095. Www.Ijmer.Com.
[72] N. Gewili, A.M. Abdelghany, M. Mekhaimer, A. Oraby, Synthesis and optical properties of chitosan/polypyrrole composite for biological applications, Lett. Appl. NanoBioSci. 10 (2021) 2742–2749, https://doi.org/10.33263/LIANBS104.27422749.
[73] M. Naguib, M. Kurtoglu, V. Presser, J. Lu, J. Niu, M. Heon, L. Hultman, Y. Gogotsi, M.W. Barsoum, Two-dimensional nanocrystals produced by exfoliation of Ti 3AlC 2, Adv. Mater. 23 (2011) 4248–4253, https://doi.org/10.1002/adma.201102306.
[74] A.A.A. Jafry, G. Krishnan, N. Kasim, N.F. Zulkipli, F.S.M. Samsamnun, R. Apsari, S. W. Harun, MXene Ti3C2Tx as a passive Q-switcher for erbium-doped fiber laser, Opt. Fiber Technol. 58 (2020), https://doi.org/10.1016/j.yofte.2020.102289.
[75] V. Sharma, A. Kumar, A. Kumar, V. Krishnan, Enhanced photocatalytic activity of two dimensional ternary nanocomposites of ZnO–Bi2WO6–Ti3C2 MXene under natural sunlight irradiation, Chemosphere 287 (2022), https://doi.org/10.1016/j.chemosphere.2021.132119.
[76] R. Kumar, B.C. Maji, M. Krishnan, Synthesis of 2D material MXene from Ti3AlC2 MAX-phase for electromagnetic shielding applications, AIP Conf. Proc. (2020), https://doi.org/10.1063/5.0025338.
[77] Erratum, Study of Chitosan-Stabilized Ti3C2Tx MXene for Ultrasensitive and Interference-Free Detection of Gaseous H2O2 (ACS Applied Materials and Interfaces) 15:26, 2023, pp. 31643–31651, https://doi.org/10.1021/acsami.3c05314. ACS Applied Materials and Interfaces. 15 (2023) 39025. doi: 10.1021/acsami.3c10281.
[78] T. Qiang, B. Qiu, L. Chen, L. Ren, Carboxylated chitosan modified alkalization of 2D MXene Ti3C2 and its Cr(VI) removal performance in aqueous solution, Ceram. Int. 49 (2023) 6688–6698, https://doi.org/10.1016/j.ceramint.2022.10.272.
[79] E.A. Elizalde-Peña, N. Flores-Ramirez, G. Luna-Barcenas, S.R. Vásquez-García, G. Arámbula-Villa, B. García-Gaitán, J.G. Rutiaga-Quiñones, J. González-Hernández, Synthesis and characterization of chitosan-g-glycidyl methacrylate with methyl methacrylate, Eur. Polym. J. 43 (2007) 3963–3969, https://doi.org/10.1016/j.eurpolymj.2007.06.004.
[80] S. Wei, Y. Xie, Y. Xing, L. Wang, H. Ye, X. Xiong, S. Wang, K. Han, Two-dimensional graphene oxide/MXene composite lamellar membranes for efficient solvent permeation and molecular separation, J. Membr. Sci. 582 (2019) 414–422, https://doi.org/10.1016/j.memsci.2019.03.085.
[81] K. Huang, G. Liu, Y. Lou, Z. Dong, J. Shen, W. Jin, A graphene oxide membrane with highly selective molecular separation of aqueous organic solution, Angewandte Chemie - International Edition. 53 (2014) 6929–6932, https://doi.org/10.1002/anie.201401061.
[82] Y. Liu, M. Zhu, M. Chen, L. Ma, B. Yang, L. Li, W. Tu, A polydopamine-modified reduced graphene oxide (RGO)/MOFs nanocomposite with fast rejection capacity for organic dye, Chem. Eng. J. 359 (2019) 47–57, https://doi.org/10.1016/j.cej.2018.11.105.
[83] Y. Dong, J. Liu, Y. Chen, T. Zhu, Y. Li, C. Zhang, X. Zeng, Q. Chen, Q. Peng, Photothermal and natural activity-based synergistic antibacterial effects of Ti3C2Tx MXene-loaded chitosan hydrogel against methicillin-resistant Staphylococcus aureus, Int. J. Biol. Macromol. 240 (2023), https://doi.org/10.1016/j.ijbiomac.2023.124482.
[84] A. Rozmysłowska-Wojciechowska, E. Karwowska, M. Gloc, J. Woźniak, M. Petrus, B. Przybyszewski, T. Wojciechowski, A.M. Jastrzębska, Controlling the porosity and biocidal properties of the chitosan-hyaluronate matrix hydrogel nanocomposites by the addition of 2D Ti3 C2 Tx mxene, Materials 13 (2020) 1–16, https://doi.org/10.3390/ma13204587.
[85] X. Kang, Y. Li, Z. Duan, X. Shen, R. Fu, D. Fan, A Mxene@TA/Fe dual-nanozyme composited antifouling hydrogel for burn wound repair, Chem. Eng. J. 476 (2023), https://doi.org/10.1016/j.cej.2023.146420.
[86] H. Wang, A. Dong, K. Hu, W. Sun, J. Wang, L. Han, L. Mo, L. Li, W. Zhang, Y. Guo, L. Zhu, F. Cui, Y. Wei, LBL assembly of Ag@Ti3C2T Xand chitosan on PLLA substrate to enhance antibacterial and biocompatibility, Biomed. Mater. (Bristol). 17 (2022), https://doi.org/10.1088/1748-605X/ac62e7.
[87] L. Guo, K. Hu, H. Wang, Antimicrobial and mechanical properties of ag@Ti3C2Tx-modified PVA composite hydrogels enhanced with quaternary ammonium chitosan, Polymers 15 (2023), https://doi.org/10.3390/polym15102352.
[88] N.H. Al-Garah, F.L. Rashid, A. Hadi, A. Hashim, Synthesis and characterization of novel (organic-inorganic) nanofluids for antibacterial, antifungal and heat transfer applications, J. Bionanosci. 12 (2018) 1–5, https://doi.org/10.1166/jbns.2018.1538.
[89] H. Li, Y. Yang, M. Mu, C. Feng, D. Chuan, Y. Ren, X. Wang, R. Fan, J. Yan, G. Guo, MXene-based polysaccharide aerogel with multifunctional enduring antimicrobial effects for infected wound healing, Int. J. Biol. Macromol. 261 (2024), https://doi.org/10.1016/j.ijbiomac.2024.129238.
[90] W.S. Khan, S. Pyarasani, R. Asmatulu, Reinforcing antibacterial hydrogels through electrospun nanofiber layers for soft tissue engineering, J. Polym. Res. 27 (2020), https://doi.org/10.1007/s10965-020-02354-4.
[91] K.T.L. Trinh, D.A. Thai, D.H. Yang, N.Y. Lee, Chitosan: a green adhesive for surface functionalization and fabrication of thermoplastic biomedical microdevices, Lab Chip 23 (2023) 4245–4254, https://doi.org/10.1039/d3lc00500c.
[92] L. Zhang, H. Zhang, H. Zhou, Y. Tan, Z. Zhang, W. Yang, L. Zhao, Z. Zhao, A Ti3C2 MXene-integrated near-infrared-responsive multifunctional porous scaffold for infected bone defect repair, J. Mater. Chem. B 12 (2023) 79–96, https://doi.org/10.1039/d3tb01578e.
[93] L. Mao, S. Hu, Y. Gao, L. Wang, W. Zhao, L. Fu, H. Cheng, L. Xia, S. Xie, W. Ye, Z. Shi, G. Yang, Biodegradable and electroactive regenerated bacterial cellulose/MXene (Ti3C2Tx) composite hydrogel as wound dressing for accelerating skin wound healing under electrical stimulation, Adv. Healthc. Mater. 9 (2020), https://doi.org/10.1002/adhm.202000872.
[94] F. Cheng, X. Yi, J. Dai, Z. Fan, J. He, Y. Huang, H. Li, Photothermal MXene@Zn-MOF-decorated bacterial cellulose-based hydrogel wound dressing for infectious wound healing, Cell Reports Phys. Sci. 4 (2023), https://doi.org/10.1016/j.xcrp.2023.101619.
[95] K. Kadhim, I. Agool, A. Hashim, Synthesis of (PVA-PEG-PVP-TiO 2) nanocomposites for antibacterial application, Mater. Focus. 5 (2016) 436–439, https://doi.org/10.1166/mat.2016.1371.
[96] M. Ahamed, M.J. Akhtar, M.A.M. Khan, P. Karuppiah, Antibacterial, antifungal, and anticancer potential of two-dimensional Ti3C2Tx MXene, Mater. Lett. 327 (2022), https://doi.org/10.1016/j.matlet.2022.133020.
[97] T. Wojciechowski, A.M. Jastrzębska, A.S. Vasilchenko, M. Jakubczak, M. Wolska-Pietkiewicz, A. Rozmysłowska-Wojciechowska, D. Moszczyńska, A. Olszyna, W. Ziemkowska, Non-toxic 2D Ti3C2 MXene surface-modified with Al, Ga, In alkoxides by chemical reactions with metal trialkyls, Nano-Struct. Nano-Obj. 29 (2022), https://doi.org/10.1016/j.nanoso.2021.100820.